3-D Interactions between a Finite-Span Synthetic Jet and a Cross-Flow

by

Joshua VanDuyn Wood

A Thesis Submitted to the Graduate

Faculty of Rensselaer Polytechnic Institute

in Partial Fulfillment of the

Requirements for the degree of

MASTER OF SCIENCE

Major Subject: AERONAUTICAL ENGINEERING

Approved by the
Examining Committee:

____
Michael Amitay, Thesis Adviser

____
Assad Oberai, Member

____
Luciano Castillo, Member

Rensselaer Polytechnic Institute
Troy, New York

August, 2011

CONTENTS

LIST OF FIGURES iv

ACKNOWLEDGMENT vii

ABSTRACT viii

1. Introduction and Historical Review 1

    1.1 Synthetic Jets in Quiescent Conditions 3

    1.2 Low Aspect Ratio Synthetic Jets in a Cross-Flow 5

    1.3 Finite-Span Rectangular Synthetic Jets in a Cross-Flow 8

2. Experimental Setup 10

    2.1 RPI Subsonic Research Wind Tunnel 10

    2.2 Synthetic Jet Actuators 10

        2.2.1 Actuator Design 11

        2.2.2 Synthetic Jet Calibration 12

    2.3 Experimental Model 14

    2.4 Particle Image Velocimetry Measurements 16

        2.4.1 Two Dimensional Particle Image Velocimetry 17

        2.4.2 Stereo Particle Image Velocimetry 18

3. Results 21

    3.1 Reynolds Number and Angle of Attack Effect 21

    3.2 Quasi-Periodic Flow along the Mid-Span: Actuated Cases 24

    3.3 Time-Averaged Flow Field 26

    3.4 Phase-Averaged Flow Field 33

    3.5 Triple Decomposition 41

4. Discussion and Conclusions 46

5. Future Work 48

6. References 49

LIST OF FIGURES

2.1: Diagram of a synthetic jet actuator in quiescent air 10

2.2: Actuator cavity dimensions 12

2.3: Dantec hotwire positioned in jet orifice for actuator calibration. 13

2.4: Jet peak velocity versus actuation frequency, for seven voltages 14

2.5: Picture of the wind tunnel model with three modules of synthetic jets along the span and chord. 15

2.6: Model mounted inside the wind tunnel, showing the root fence and the sidewall... 16

2.7: Picture of the center module, with three rows of jets and five jets in each row, front side (left) and backside (middle). On the right, PIV measurement planes at jet 3; solid lines represent planes on which data were acquired while dashed lines represent mirrored planes. 20

3.1: Total velocity data for baseline (a-c) and forced cases with C_b = 1.2 (d-f) at 10^0 angle of attack. Reynolds numbers of 50,000 (a, d), 100,000 (b,e), and 250,000 (c,f) are shown. 22

3.2: Total velocity data for baseline (a-c) and forced cases with C_b = 1.2 (d-f) at 18^0 angle of attack. Reynolds numbers of 50,000 (a, d), 100,000 (b,e), and 250,000 (c,f) are shown. 23

3.3: Experimental data of time-averaged total velocity (a-c) and phase-averaged spanwise vorticity (d-f) fields across the center-plane of jets 2 (a, d), 3 (b, e), and 4 (c,f). 25

3.4: Contour plot of the total velocity across the center-plane of jet 3; time-averaged total velocity profiles along five lines normal to the surface at x/h = -3 (line A), -1.5 (line B), 0 (line C at jet exit), 1.5 (line D), and 3 (line E). Velocity profile on subsequent lines are offset by a unit distance of $U/U_\infty = 1$ 27

3.5: Contour plots of the total velocity across the center-plane of jet 3; Forced cases with C_b = 0.4 (a) and 1.2 (b). 28

3.6: Time-averaged total velocity profiles along five lines normal to the surface at x/h = -3 (line A), -1.5 (line B), 0 (line C at jet exit), 1.5 (line D), and 3 (line E). Forced cases with C_b = 0.4 (a) and 1.2 (b). 30

3.7: Effect of the momentum coefficient on the time-averaged (volumetric) flow field; experimental data for six actuated cases; C_b = 0.2 (a), 0.4 (b), 0.6 (c), 0.8 (d), 1.0 (e), and 1.2 (f). Iso-surface of total velocity at U/U_∞ = 1.3. 32

3.8: Center-plane phase-averaged span-wise vorticity for an actuated case with C_b = 0.4 at two phases; $\phi = 120^0$ (a) and 240^0 (b). Lighter shade is used for CW vorticity while darker for CCW vorticity. 34

3.9: Center-plane phase-averaged spanwise vorticity for an actuated case with C_b = 1.2 at two phases; $\phi = 120^0$ (a) and 240^0 (b). Shades are same as in Figure 3.8. 35

3.10: Iso-surfaces of phase-averaged spanwise vorticity $|\Omega_z|c/ U_\infty$ = 30.5; one in clockwise sense (in light shade) and other in counter-clockwise sense (in dark shade). For an actuated case with C_b = 0.4 at two phases; $\phi = 120^0$ (a) and 240^0 (b). 36

3.11: Iso-surfaces of phase-averaged spanwise vorticity $|\Omega_z|c/ U_\infty$ = 30.5; one in clockwise sense (in light shade) and other in counter-clockwise sense (in dark shade). For an actuated case with C_b = 1.2 at two phases; $\phi = 120^0$ (a) and 240^0 (b). 36

3.12: Phase-averaged spanwise vorticity based on experimental data on center-plane for three actuated cases with C_b = 0.4 (a-f), 0.8 (g-l), and 1.2 (m-r). Six different phases (at every 60^0 starting from 180^0 at the top most row) are considered to show temporal evolution and interactions of vortical structures. 38

3.13: Spanwise vorticity, instantaneous (a,b) and phase-averaged (c,d), based on numerical data at center-plane for two actuated cases with C_b = 0.4 (a,c) and 1.2 (b,d) at a phase of 240^0. Shades are same as in Figure 13. Courtesy of Sahni and Jansen. 40

3.14: Iso-surfaces of spanwise vorticity, instantaneous (left-half of span in each case) and phase-averaged (right-half of span), with equal but opposite values of $|\Omega_z|c/ U_\infty$ = 30.5 (light shade is used for CW vorticity and dark shade for CCW). Numerical data is shown for two actuated cases with C_b = 0.4 (a, c) and 1.2 (b, d) at two phases; $\phi = 120^0$ (a, b) and 240^0 (c, d). Lines in the mid-span depict the center-plane. Courtesy of Sahni and Jansen. 41

3.15: Black and white contour plots of the dimensionless normal stresses of the streamwise component (a-c), the normal component (d-f) and the shear stresses (g-i); total stresses (a, d, g), coherent stresses (b, e, h) and random stresses (c, f, i) at C_b = 1.2 and Re_c = 100,000. 43
3.16: Black and while contour plots of the normalized total (a), coherent (b), and random turbulent kinetic energy (c) at C_b = 1.2 and Re_c = 100,000...................................... 45

ACKNOWLEDGMENT

This work has been supported by the AFOSR, under grant number FA9550-08-1-0233, monitored by Drs. John Schmisseur and Douglas Smith. I would like to thank my advisor, Prof. Michael Amitay, for giving me the opportunity to conduct this research and the guidance to carry it through, as well as Profs. Onkar Sahni and Kenneth Jansen, for the numerical simulations and many of the figures. My fellow graduate students have also been indispensible in both their knowledge and comradeship, making the lab into a place of discussion and learning. Furthermore, undergraduate student Mr. Kevin Mossey must be recognized for his tremendous help in organizing and processing of the experimental data. I would also like to acknowledge the insightful discussions provided by Dr. Yossef Elimelech along with the help of undergraduate students Mr. Dan Finigan and Ms. Meghan Lenihan.

ABSTRACT

An experimental investigation was performed to study the formation of secondary flow structures and interactions of a finite-span synthetic jet in a cross-flow at chord-based Reynolds numbers between 50,000 and 400,000 and angles of attack from 0^0 to 20^0. Six blowing ratios, in the range of 0.2 to 1.2 with an increment of 0.2 (where, the blowing ratio is defined based on the averaged outstroke jet velocity to the free-stream velocity) were tested. Experiments were conducted on a finite wing (aspect ratio of 5.33) with a cross-sectional profile of NACA 4421, where both 2-D and stereoscopic PIV data were collected at the center jet in the mid-span. The effect of the blowing ratio was analyzed based on 3-D time-averaged, phase-averaged and instantaneous flow fields at an angle of attack of 0^o and a chord Reynolds number of 100,000. For the low blowing ratio cases, spatial non-uniformities developed, due to the finite-span of the slit, which led to the formation of small and organized secondary structures or a streak-like pattern in the mean flow. On the other hand, for the high blowing ratio range turbulent vortical structures were dominant leading to larger spanwise structures, with a larger spanwise wavelength, in the mean flow. Moreover, the phase-locked flow fields exhibited a train of counter-rotating coherent vortices that lifted-off the surface as they advected downstream. In the mid-blowing ratio range, combined features of the low-range (near the slit) and high-range (in downstream locations) were found; where a pair of counter-rotating vortices issued in the same jet cycle collided with each other. To explore whether the flow is dominated by random or coherent motions, a large number of phase averages (36) flow fields were acquired, along with a time average of the same case, and a triple decomposition was performed. The coherent motions were shown to exist only near the orifice and the path of the vortex train, while the random motions were farther downstream (where the vortex train diminishes). In all cases the spanwise extent of the secondary coherent structures reduced with downstream distance with a larger decrease at higher blowing ratios. Similar observations were made in earlier studies on finite-span synthetic jets in quiescent conditions.

1. Introduction and Historical Review[1]

The major goal in aerodynamics is to improve vehicle performance over a wide range of operating conditions. This can be achieved by optimizing the shape, or by using passive and/or active flow control techniques. Active flow control techniques based on fluidic actuators have been widely studied and used due to their dynamic applicability over a broad range of flow conditions along with their efficiency (e.g., separation mitigation at high angles of attack, virtual aero-shaping at low angles of attack, etc.). One approach is to couple the actuation frequency to instabilities inherent to separated flows and thus, alter the global flow field by modifying the large-scale vortical structures, e.g., Oster & Wygnanski (1982), Ho & Huerre (1984), Roberts (1985), Seifert et. al. (1993), Wygnanski (2000). In this approach, the time-period of actuation scales with the advection time through the length of the flow domain downstream of the separation (as measured by the reduced or non-dimensional frequency, F^+). In such an approach, control input is effective within a limited spatial domain immediately upstream of separation; however, when the flow is not separated (e.g., at low angles of attack) the efficacy of this approach is negligible (e.g., Seifert et al., 1993).

A different approach, where fluidic actuators that are driven at much larger frequencies than characteristic flow frequencies (such as synthetic jets, e.g., Amitay & Glezer, 2002a; Glezer et. al., 2005), allows more control through the modification of the apparent aerodynamic shape of the lifting surfaces (e.g., Amitay et. al., 1997; Amitay et. al., 2001b). This approach does not necessarily rely on coupling the actuation frequency to global flow instabilities and therefore, can be applied at various spatial locations and over a broader range of flow conditions (e.g., Amitay et. al., 2001a; Glezer & Amitay, 2002). Furthermore, it can accommodate a broader band control algorithms where more

[1] Portions of this chapter previously appeared as: Sahni, O., Wood, J., Jansen, K.E. & Amitay, M. (2011). Three Dimensional Interactions between a Finite-Span Synthetic Jet and a Cross-Flow. *Journal of Fluid Mechanics*, *671*, 254-287.

complex actuation waveforms can be used (e.g., the pulse modulation technique, Amitay & Glezer, 2006).

In the last decade a variety of promising flow control applications based on synthetic jet actuators have been presented. Several studies on synthetic jet applications have demonstrated that flow separation can be mitigated or even suppressed altogether (e.g., see Amitay et. al., 1999; Amitay & Glezer, 2002b; Crook et. al., 1999; He et. al., 2001). Synthetic jets have also been used for separation control in inlet ducts (e.g., Amitay et. al., 2002c). It has also been demonstrated on unmanned aerial vehicle (e.g., Parekh et. al., 2003), jet vectoring (e.g., Smith & Glezer, 2002) as well as for flight control on scaled models (e.g., Ciuryla et. al., 2007). More recently it has been used for vibration suppression in wind turbines by Maldonado et. al. (2009). Synthetic jets have also been applied at low angles of attack, where the flow is fully attached, for 2-D platforms (e.g., Chatlynne et. al., 2001; Amitay et. al., 2001a) and also for 3-D configurations (e.g., Farnsworth et. al., 2008). In some studies significant control forces were imparted by cropping the trailing edge of an airfoil and using synthetic jets (e.g., Timor et. al., 2007); which indicates an opportunity to replace the conventional control surfaces (e.g., flaps, aileron, rudder, etc.) with active flow control, or at least augment their performance in terms of control authority as well as frequency response.

Apart from such attractive synthetic jet based flow control applications, a large number of studies have been performed to investigate and characterize the flow structures and mechanisms due to synthetic jet actuation. These studies were experimental, computational or combined. More importantly, these investigations can be classified into two broad classes: (a) synthetic jets in quiescent conditions, and (b) synthetic jets in a cross-flow. Furthermore, these studies involved synthetic jets that were issued through orifices of different geometry ranging between: (i) plane 2-D or very high aspect ratio slits, minimizing the end effects (i.e., with aspect ratios of 75 or above), (ii) circular, elliptic or low aspect ratio ones (with aspect ratios below 5), and (iii) finite-span or rectangular slits with end effects (i.e., with aspect ratios between 5 and 75). Therefore, in the balance of this introduction three categories are considered and discussed: (1) synthetic jets in quiescent conditions (including circular, elliptic or rectangular slits covering full range of aspect ratios), (2) low aspect ratio synthetic jets in a cross-flow, and (3) finite-span rectangular synthetic jets in a cross-flow. The rational for this categorization is that the majority of the existing studies, to the best of the author's knowledge, lie in the realm of the first two categories. On the other hand, flow structures formed due to the finite-span of rectangular synthetic jets can play an important role in various flow control applications (e.g., separation control, virtual aero-shaping, etc.) and require deeper understanding; therefore, it is the focus of the present work.

1.1 Synthetic Jets in Quiescent Conditions

Smith & Glezer (1998) were the first to experimentally study the flow field of a synthetic jet in quiescent conditions (i.e., without a cross-flow). In their study, the jet was issued via a rectangular slit of a very high aspect ratio (i.e., 150). They showed, using spanwise flow visualization along the long axis of the slit, that periodically formed discrete vortex pairs undergo a transition to turbulence in a jet cycle and lose their coherence due to formation of instabilities in the form of spanwise-regular rib-like secondary vortical structures.

Numerical investigations of synthetic jet in quiescent conditions were performed by Kral et. al. (1997) and Lee & Goldstein (2002) based on 2-D simulations while Rizzetta et. al. (1999) performed high-resolution 3-D simulations. Note that in the 3-D simulations by Rizzetta et. al. (1999), the spanwise length of the slit was reduced by a factor of 10 as compared to the experiments of Smith & Glezer (1998) and furthermore, symmetry conditions at the jet centerline and mid-span were used to include only one quarter of the physical configuration; this was done due to limitation on computing resources. Two-dimensional simulations agreed with the experiments near the exit of the jets where the flow field was dominated by counter-rotating vortex pairs while farther away from the jet slit (i.e., after 10 slit widths) there was significant disagreement. On the other hand, 3-D simulations (by Rizzetta et. al., 1999) captured spanwise instabilities, which led the counter-rotating vortex pair to lose their coherence and breakdown farther downstream as was observed in the experiments (even though it was not possible in 3-D simulations to exactly duplicate the experimental configuration in terms of spanwise length of the jet slit). Mallinson et. al. (1999), Crook & Wood (2001), Cater & Soria (2002), and Zaman & Milanovic (2003) also made similar observations on 3-D flow structures and instabilities for synthetic jets issued through a circular orifice.

More recently, Yao et. al. (2004) conducted detailed experimental measurements of synthetic jets in quiescent conditions to be used for validation studies. The synthetic jet in this case had a rectangular slit with an aspect ratio of 28. Measurements were made using three different techniques, namely, Particle Image Velocimetry (PIV), Laser Doppler Velocimetry (LDV), and hot-wire anemometry; which included both near- and far-field measurements as well as measurements on two planes along and across the slit. They showed that besides the end effects at the edge of the jet slit, 3-D flow structures develop due to spanwise instabilities when the jet is advected downstream. They noted, as was done by Smith & Glezer (1998), that near the jet slit flow behavior is relatively smooth and uniform while the jet front develops wavy profiles downstream.

Numerical investigations for this case were done with varying degrees of success; which were based on 2-D and 3-D simulations. As before, in contrast to 2-D simulations, high-resolution 3-D simulations were able to capture spanwise instabilities in the form of rib-like secondary structures in the primary vortex pair, see Kotapati et. al. (2007) (they did not model the end effects by considering a jet along the entire span of the computational domain). Cui & Agarwal (2006) also performed 3-D simulations and included slot ends but showed limited agreement with the experiments which is possibly because the grid used was fairly coarse with only 29 points along the spanwise length of the slit (note that the aspect ratio of the slit is 28). For a detailed survey of simulations for this case see Rumsey (2009).

Amitay & Cannelle (2006) also carried out detailed experimental measurements for finite-span synthetic jets (i.e., issued via rectangular slits) in quiescent conditions, where they collected PIV data on two planes across and along the slit. They considered a range of orifice aspect ratios (from 50.8 to 101.6) and synthetic jet parameters (including stroke length and actuation frequency). Similar to earlier studies they showed that vortex pairs near the jet orifice are uniform and 2-D but farther downstream develop horseshoe-like patterns with secondary counter-rotating vortical structures along the span that form an array of streaks in the mean flow. They also showed the presence of edge-induced vortices due to the finite span of the slit as well as 3-D instabilities that prevail in the mid-span of the jet (even for a case with aspect ratio of 101.6; as was visualized by Smith & Glezer, 1998). Cannelle & Amitay (2007) extended these studies to investigate the transitory behavior of synthetic jets (following the onset and termination of the actuation), where they also made hot-wire measurements, and showed the formation, evolution and merging of vortices in the cross-stream and spanwise planes.

1.2 Low Aspect Ratio Synthetic Jets in a Cross-Flow

In addition to detailed investigations of synthetic jets issued into a quiescent flow, the second category of studies involves synthetic jets in a cross-flow. Such studies, leading to understanding and characterization of flow structures and interactions due to synthetic jet actuation in the cross-flow, are critical for their effective application in flow environments of practical interest. Most of the studies on synthetic jets in a cross-flow have considered circular or elliptic orifices (with low aspect ratio). Crook & Wood (2001) used a water tunnel and studied an isolated circular synthetic jet in a cross-flow along with an array of synthetic jets on a tripped circular cylinder. In their experiments, they used dye visualization to show the 3-D interactions of vortical structures due to their tilting, stretching and mutual interaction. Similarly, Sauerwein & Vakili (1999) studied 3-D interactions of vortex rings for several synthetic jet configurations in a water tunnel. Gordon & Soria (2002) also used a water tunnel and carried out PIV measurements for a circular synthetic jet in a cross-flow. They considered only one measurement plane located at the center of the orifice and aligned with the cross-flow; based on this PIV data they observed deflection in the mean streamlines of the cross-flow to be up to 2-3 orifice diameters from the wall and for a distance up to 15-20 diameters.

Zaman & Milanovic (2003) used hot-wire anemometry in wind tunnel experiments to study a circular synthetic jet in a turbulent boundary layer and showed the formation of counter-rotating vortex pair, a region of low-momentum downstream to the jet (due to the blockage caused by the jet), and also high turbulence intensity regions. Milanovic & Zaman (2003) further extended their investigation to orifices of different geometries, including straight, tapered, pitched and clustered jet slots, all with the same cross-section at the slit. For the most part they observed similar flow structures between different orifices. The differences were in the jet penetration, which was somewhat smaller in the case of pitched and clustered orifices, and as expected, the pitched jet also lead to a region of high-momentum near the wall. In another study, Milanovic et. al. (2005) carried out a joint experimental and computational investigation of a straight circular synthetic jet in a cross-flow. They showed the overall agreement to be good in both axial and traverse planes but computational results over predicted the extent of the velocity deficit regions.

Schaeffler (2006) carried out detailed measurements, including LDV as well as planar- and stereoscopic PIV, for a circular synthetic jet in a turbulent cross-flow to be used as a validation database (similar to the case of a synthetic jet in quiescent conditions by Yao et. al., 2004). They showed same features of deflection in the mean streamlines of the cross-flow in the axial symmetry plane and counter-rotating vortex pair in the traverse plane. As before, follow up numerical studies, including 2-D and 3-D simulations, were carried out for this case. Three-dimensional simulations showed a reasonable qualitative agreement with experiments (e.g., see Cui & Agarwal, 2005; Dandois et. al., 2006); for a survey of numerical simulations for this case see Rumsey (2009).

Other detailed experimental studies on circular synthetic jets in a cross-flow were carried out recently by Jabbal & Zhong (2008), and Iai et. al. (2009); all of which were conducted in a laminar or a low Reynolds number cross-flow. Jabbal & Zhong (2008) used a water tunnel to investigate the flow field of a circular synthetic jet on a flat plate. They carried out measurements based on stereoscopic dye visualization and thermochromic liquid crystal-based convective heat transfer sensing system to detect thermal footprints of passing flow structures. They identified three different types of vortical structures based on the range of blowing ratio, namely, hairpin vortices, stretched vortex rings, and tilted/distorted vortex rings. Furthermore, based on the thermal footprints of the flow structures they conjectured that either hairpin vortices or stretched vortex rings was responsible for the delayed separation on the circular cylinder studied by Crook et. al. (2001). Study by Iai et. al. (2009) was carried out in a fully developed low Reynolds number channel flow, which included a circular synthetic jet oriented either perpendicular to the cross-flow or with a 45^0 pitch. Their measurements were based on scanning stereoscopic PIV system with multiple planes along the span to construct a 3-D flow field (similar to the technique used in the present study). One blowing ratio for both configurations of the synthetic jet was considered and formation of hairpin vortex structure was observed. As expected, in the inclined configuration asymmetry existed in the two longitudinal vortices of the hairpin structure.

More validations studies on the interaction of circular synthetic jets with a cross-flow include Zhou & Zhong (2009) and Wu et. al. (2009). Zhou & Zhong (2009) showed a good agreement with the laminar case of Jabbal & Zhong (2008), whereas Wu et. al. (2009) considered a turbulent cross-flow over a flat plate and showed a reasonably good agreement at downstream locations. Numerical studies were also carried out ranging from 2-D to 3-D simulations. For example, Mittal et. al. (2001) and Mittal & Rampunggoon (2002) performed 2-D simulations of synthetic jets in a laminar flow over a flat plate, and showed the existence of recirculation bubble in the mean flow near the orifice to demonstrate the virtual aero-shaping effect, whereas Ravi et. al. (2004) investigated effects of square and rectangular orifices (with aspect ratio up to 4) based on 3-D simulations; however, they presented limited results due to constraints on computing resources.

1.3 Finite-Span Rectangular Synthetic Jets in a Cross-Flow

Smith (2002) performed wind tunnel experiments on an array of finite-span synthetic jets in a turbulent boundary layer (each jet had a rectangular orifice with an aspect ratio of 45). Two configurations of three parallel synthetic jets aligned in spanwise and streamwise directions on a flat plate were considered. All the measurements were based on hot-wire anemometry and therefore, it was noted that understanding 3-D flow structures in detail was difficult. Nevertheless, prominent features were shown, for example, spanwise configuration with an orifice normal to the cross-flow showed the blockage caused just upstream of the orifice along with a wake-like feature in the downstream region. Moreover, the orifice aligned in the streamwise direction exhibited longitudinal vortices embedded in the boundary layer.

Gilarranz et. al. (2005) also carried out wind tunnel experiments on finite-span synthetic jets (with an aspect ratio of 22.35) over a NACA 0015 wing with an aspect ratio of about 1 (end plates were used to minimize the 3-D effects due to finite span of the wing). They considered a high Reynolds number (i.e., 890,000) and varied angle of attack from low to high (i.e., -2^0 to 29^0). Their results were based on force balance measurements, on-surface oil flow visualization, smoke flow visualization, surface pressure measurements, and wake surveys. Based on these measurements they showed significant effects due to synthetic jet actuation at high angles of attack, where the onset of stall was delayed from 12^0 to 18^0 and up to 80% increase in the lift coefficient was observed. They also showed a decrease in drag due to synthetic jet actuation. Recently, You and Moin (2008) numerically simulated this case at the same Reynolds number and at an angle of attack of 16.6^0. In their 3-D simulations, they considered the jet slit to cover the entire span of the computational domain and thus, eliminating the end effects. They showed good agreement for the lift-coefficient and the wake. Furthermore, they presented phase-averaged velocity profiles, streamlines and pressure field, and also instantaneous iso-surfaces of vorticity, which helped in understanding the interaction of the jet with the cross-flow but without any end effects.

The motivation of the present paper is to extend the understanding of a finite-span synthetic jet interaction with a cross-flow; specifically, to investigate and explore the formation and evolution of secondary flow structures in the vicinity of the jet. In the present work, a low chord-based Reynolds number of 100,000 and 0^0 angle of attack were selected. Also note that the jet was located near the leading edge at 17% of the chord (i.e., near the suction peak). Thus, the synthetic jet experienced a cross-flow with an oncoming boundary layer that was attached and laminar as it developed over the airfoil in a region with a strong favorable pressure gradient. Nevertheless, flow structures due to synthetic jet at high blowing ratio cases were found to be turbulent in downstream locations (as also seen without a cross-flow, e.g., Smith & Glezer, 1998; Rizzetta et. al., 1999; Amitay & Cannelle, 2006).

An experimental study was performed, where 2-D and stereoscopic PIV measurements were carried out in the near vicinity of the synthetic jet for six different blowing ratios. The primary focus of the current investigation was to provide a detailed understanding of the flow interaction, specifically in the vicinity of the synthetic jet. The broad goal of this on-going work is to understand the flow mechanisms associated with an array of synthetic jet actuators over true 3-D platforms (e.g., finite wings with sweep and/or taper). This knowledge can then be used to efficiently implement active flow control for flight control in lieu of, or in addition to, conventional control surfaces.

2. Experimental Setup

2.1 RPI Subsonic Research Wind Tunnel

The wind tunnel experiments were conducted in the Subsonic Large Scale Research Wind Tunnel located in the Flow Control Research Laboratory at Rensselaer Polytechnic Institute (RPI). The wind tunnel was designed and built by Engineering Laboratory Design, Inc. and has been in operation since 2007. It is an open-return wind tunnel driven by a 100hp electric motor with a centrifugal blower and has a contraction area ratio of 9:1 providing a maximum velocity of ~50m/s with a maximum turbulence intensity of 0.15%. The test section has a cross-section of 80*cm* x 80*cm* and is 457*cm* long. The test section walls and floor are constructed of a 25.4mm thick acrylic glass providing an excellent optical accessibility throughout the entire test section. The experimental measurements presented here utilize a LaVision Stereoscopic Particle Image Velocimetry (SPIV) system.

2.2 Synthetic Jet Actuators

A synthetic jet, or zero-mass-flux-jet, is a jet created by pulling the ambient fluid into a cavity and then expelling it, in this research through the use of a piezo-electric disk. The jet created is unsteady and transmits only momentum into the flow. Figure 2.1 shows an image of a synthetic jet into quiescent air.

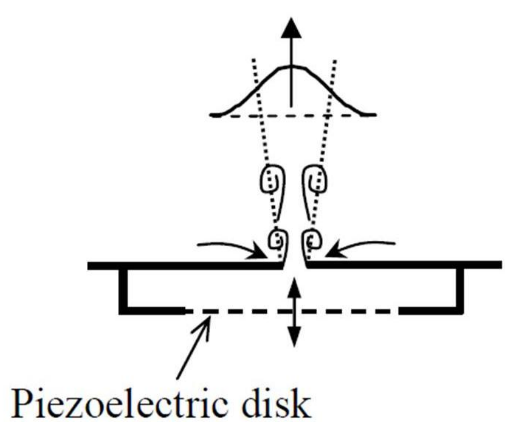

2.1: Diagram of a synthetic jet actuator in quiescent air

The strength of the synthetic jets (relative to the free-stream velocity) for incompressible flow is quantified using the momentum coefficient per jet, $C_{\mu c}$, defined as:

(1) $$C_{\mu c} = \frac{U_j^2 h}{\frac{1}{2} U_\infty^2 c}$$

where, U_∞ is the free-stream velocity, c is the wing chord, h is the width of the synthetic jet orifice, and U_j is the time-averaged jet velocity at the exit of the slot during the outstroke, defined as:

(2) $$U_j = \frac{1}{T} \int_0^{T/2} u_j t \, dt$$

where, T is the time period of the synthetic jet cycle , and $u_j(t)$ is the velocity at the center of the jet exit (measured using a hot-wire sensor in the experiments without a cross-flow). Note that the spanwise distribution of the velocity was uniform over 90% of the jet span. Another parameter used to quantify the relative strength of the synthetic jet is the blowing ratio, C_b, defined as:

(3) $$C_b = \frac{U_j}{U_\infty}$$

In the experiments, six actuation levels were selected (in addition to the baseline case), where momentum coefficient ranged from 3.96×10^{-4} to 1.42×10^{-2} (corresponding to a range of blowing ratios from 0.2 to 1.2 with an increment of 0.2); these actuation cases are labeled from $C_{\mu c1}$ to $C_{\mu c6}$. Furthermore, a frequency of 2,500*Hz* (which is not the resonance frequency of the piezoelectric disk) was selected as the driving frequency for the jets (where all the jets produced the same velocity and they all operated in-phase). Note that the characteristic frequency of the flow over the airfoil (based on the "time of flight") is about 66*Hz*, and thus, the actuation frequency is more than an order of magnitude higher, which, as will be shown later, results in a virtual aero-shaping of the wing.

2.2.1 Actuator Design

Each jet consisted of a discrete cavity and a 20mm diameter single piezoelectric disk that was mounted in the side opposite to the orifice. Each jet slot had a height of 3*mm* and was connected to a cavity chamber of a 3*mm* height and a radius of 8.75*mm* (Figure 2.2), whose size was selected by creating a cavity with a calculated Helmholtz resonance of 2500 *Hz*. The following formula was used for the design:

(4) $$f_H = \frac{v}{2\pi}\sqrt{\frac{A}{V_0 L}}$$

where f_H is the Helmholtz resonance frequency, v is the speed of sound, A is the area of the neck, V_0 is the cavity volume, and L is the length of the neck.

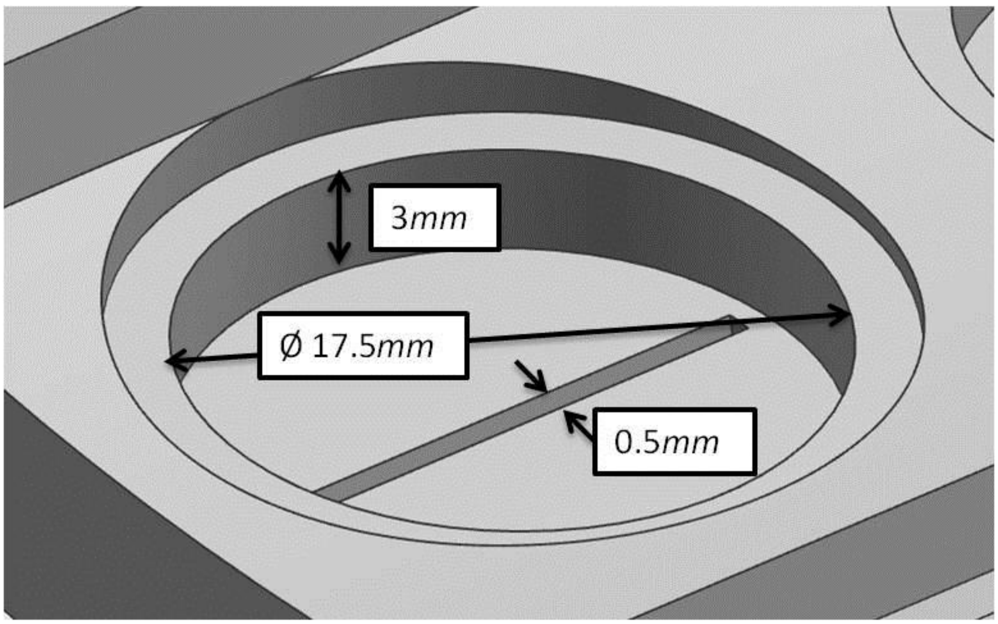

2.2: Actuator cavity dimensions

The disk (from Murata, model number: 7BB-20-3) was made of a piezoelectric material attached to a Brass substrate, and had a resonance frequency of 3,600*Hz*. The disk was attached to the cavity by applying silicone adhesive along the lip pictured in figure 2.2, pressing the disk into place, and allowing the silicone to cure for 24 hours. This provided a permanent seal that was also flexible to allow for greater disk deflection and therefore larger jet velocities.

2.2.2 Synthetic Jet Calibration

To ensure that all jets were performing well, and to allow for variations in disks and their installation, a full set of velocity versus driving voltage curves were created. The data were used to determine the ideal voltages to achieve identical jet velocities. An A.A. Labs model AN-1005 hot wire anemometry unit was used, in conjuction with a steady calibrating jet of known velocity and a Dantec 55P11 tungsten single wire, to measure synthetic jet velocity in the orifice. The measurement setup is shown in figure 2.3, where the hotwire is in position for measurement.

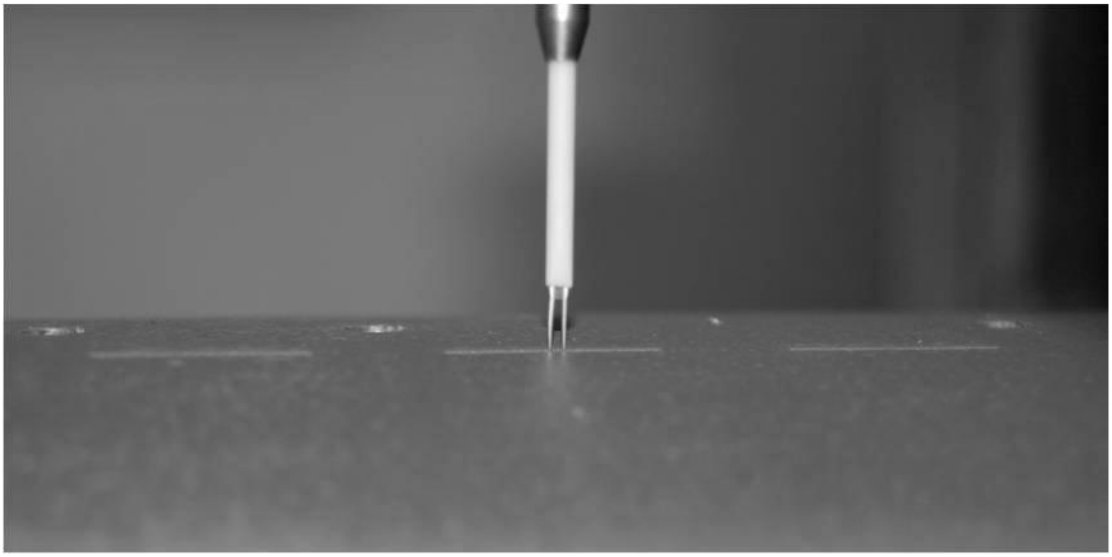

2.3: Dantec hotwire positioned in jet orifice for actuator calibration.

Due to the oscillatory nature of a synthetic jet, a Labview code was written to determine velocity peaks and find their mean, giving an average peak velocity for each case. Figure 2.4 shows a representative calibration curve, which shows that the peak velocity is obtained near the 2500*Hz* design point. The calibration curves were then compared for each jet to determine proper voltages (note that these voltages were amplified by a power amplifier, AA Lab systems model A-303, with a gain of 20) for the six blowing ratios required for experiments.

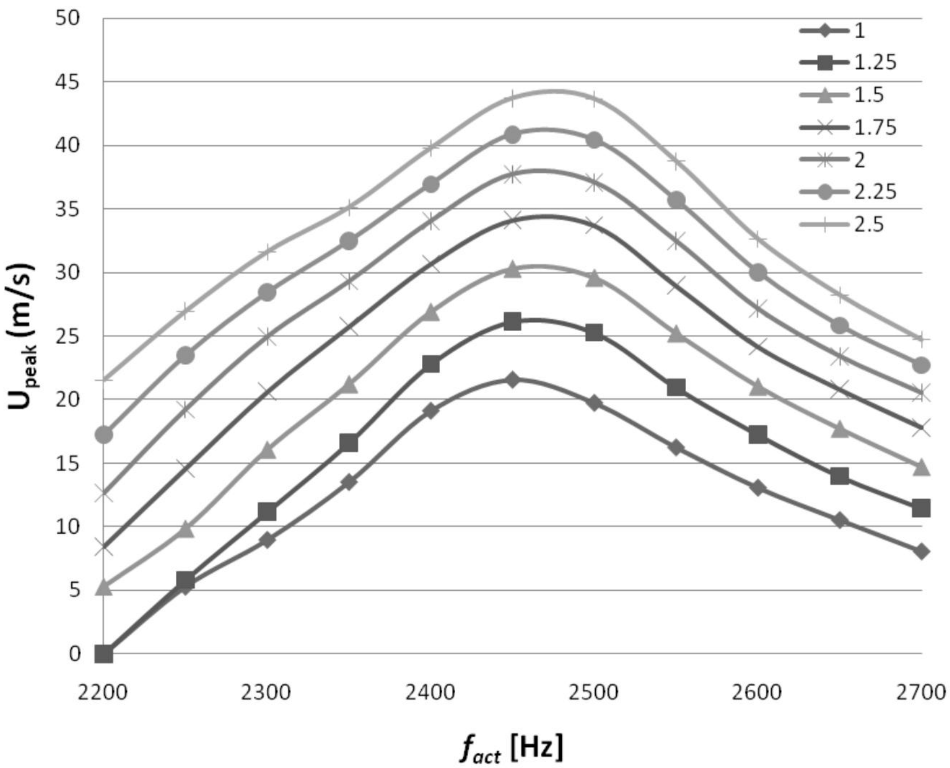

2.4: Jet peak velocity versus actuation frequency, for seven voltages

2.3 Experimental Model

The model used in the experiments was a finite wing with a constant chord, c = 15.24*cm*, and a span of b = 40.64*cm* (resulting in an aspect ratio of 5.33), and a cross-sectional shape of NACA 4421 airfoil (see Abbott & von Doenhoff, 1959). A thick airfoil was selected such that it can be instrumented with multiple synthetic jet actuators. The model was divided into three sections along the span; each was instrumented with 15 synthetic jet actuators organized in three rows (Figure 2.5). Only the first row of jets was considered in the present study, which was centered at about 17% of the chord (from the leading edge). The spanwise spacing between side edges of subsequent jets in each row is 5.4*mm*. All jet orifices were oriented perpendicular to the surface and had a length of L_z = 16*mm* (along the span), and a width of h = 0.75*mm* (in the streamwise direction), leading to an aspect ratio of 21.33.

2.5: Picture of the wind tunnel model with three modules of synthetic jets along the span and chord.

The three model sections (made by stereolithography) were attached to an aluminum skeleton. In addition, a circular fence (203.2*mm* in diameter) was placed at the root of the wing to isolate the model from the tunnel wall boundary layer. The wing assembly was attached to a motor-driven pitch mechanism to enable a precise control of the angle of attack using a belted motor and an optical encoder that ensured the accuracy of the angle of attack to +/- 0.1^0. The entire assembly was mounted in upside down configuration on one of the side walls of the wind tunnel (figure 2.6) to allow the NG-YAG laser for the PIV system to issue from below the tunnel, as the top of the tunnel is not optically accessible.

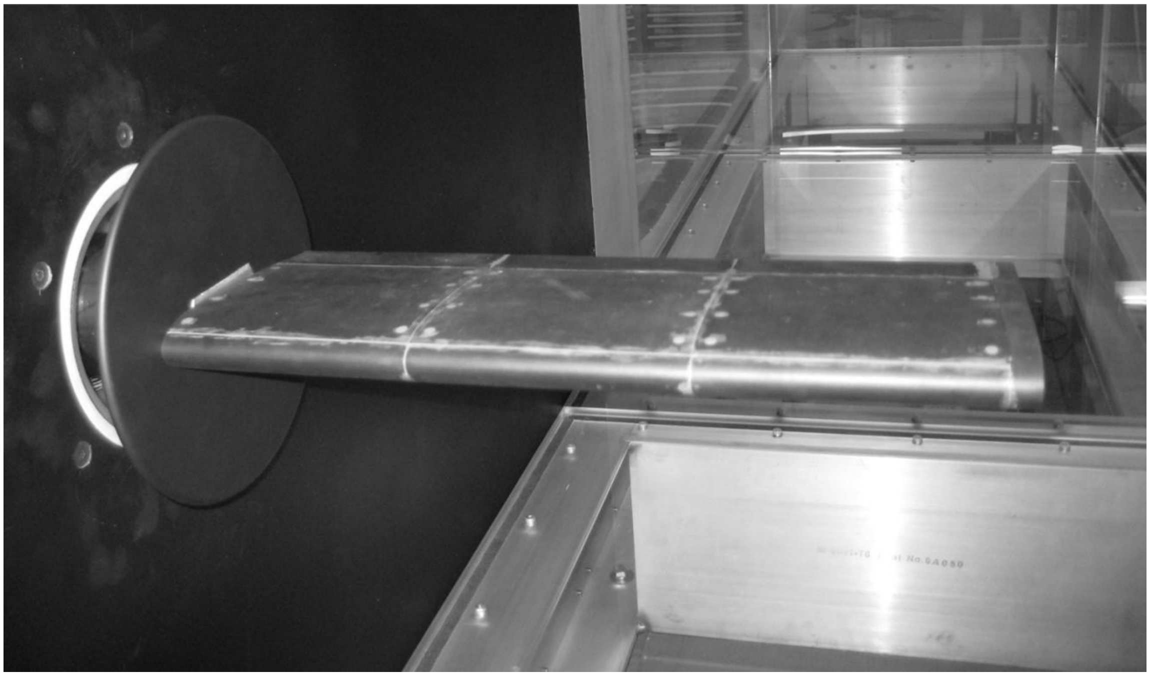

2.6: Model mounted inside the wind tunnel, showing the root fence and the sidewall.

2.4 Particle Image Velocimetry Measurements

CCD cameras were mounted on an optical table; one for the 2-D PIV and two for stereoscopic PIV. The cameras were aligned perpendicular to the laser light sheet to allow for streamwise planes to be acquired.

The PIV system used is a commercial LaVision system of hardware and software including a New Wave Solo PIV 120mJ Nd:YAG dual laser system and two 1376 x 1040 pixel resolution thermo-electrically cooled 12-bit LaVision Imager Intense CCD cameras. Cylindrical lens with a focal length of -50*mm* was used to create the light sheet and a focal lens (with a focal length range of 500*mm* to 1500*mm*) was used to focus the sheet at the measurement domain (the thickness of the light sheet at the center of the measurement domain was about 1*mm*). The laser light sheet was then aligned with the area of interest using a computer-controlled three axis traversing system mounted below the test section. The flow was seeded with O(1μm) water-based smoke particles, generated by a Martin Magnum 800 theatrical fog machine. This smoke was then injected upstream of the settling chamber to allow the particles to better mix into the flow for more complete seeding. The cameras and laser were controlled and synchronized using a LaVision PTU8 programmable timing unit.

The flow field was imaged using CCD cameras mounted on their own independently controlled three-axis traverse. The velocity components (U, V, W) were computed from the cross-correlation of pairs of successive images with 50% overlap between the interrogation domains. The images were processed using an advanced multi-pass method where the initial and final correlation passes were 64x64 pixels and 16x16 pixels, respectively. Five hundred image pairs were acquired for both the time-averaged and phase-averaged measurements. The cameras were mounted at a perpendicular distance of approximately 1*m* to the laser light, such that the distance between pixels is ~20μm. The free-stream velocity (10*m/s*) corresponds to an average displacement of approximately 8 pixels with an approximate error of ±0.1pixels, which corresponds to a maximum error of ±1.25% of the free-stream velocity (±0.125*m/s*).

2.4.1 Two Dimensional Particle Image Velocimetry

Two dimensional particle image velocimetry measurements were collected in the RPI wind tunnel focusing on the flow field at the mid span over the center jet. For the measurements the RPI LaVision Stereo PIV system was utilized, but only one camera was used. The camera was mounted such that it was parallel to the span of the airfoil and perpendicular to the laser light sheet, which was oriented vertically in the streamwise direction. A 105*mm* fixed focal length camera lens was used in conjunction with a 532nm +/- 10nm band-pass filter.

The velocity components (U_x and U_y) were computed using the cross-correlation of pairs of successive images with 50% overlap between the interrogation domains. The images were processed using an advanced multi-pass method where the initial and final correlation passes were 64x64 pixels and 32x32 pixels, respectively. Five hundred image pairs were acquired to produce the time-averaged velocity vector fields.

2.4.2 Stereo Particle Image Velocimetry

The stereoscopic particle image velocimetry measurements in the RPI wind tunnel were collected using the LaVision system previously described. Attached to an optical guiding arm either -20*mm* or -50*mm* cylindrical lenses were used to create the light sheet in conjunction with a focal lens (with a focal length range of 500*mm* to 2000*mm*) to focus the sheet at the measurement domain (the thickness of the light sheet at its waist is about 1*mm*).

The cameras were positioned to visualize the same field of view with an approximate 90^{o} angular separation between their viewing angles. The focal issues associated with the angular misalignment were then accounted for by using a Scheimpflug adapter mounted between each camera and its lens (Prasad and Jensen 1995). For the current experiments a pair of 200*mm* fixed focal length lenses were used in conjunction with a 532nm +/- 10nm band-pass filter on each of the cameras. These lenses were used to acquire streamwise plans across the jet orifices, with an interrogation window of about 25*mm* x 25*mm.*

To completely quantify the error associated with the PIV techniques a rigorous analysis of all the associated parameters is needed as discussed by Westerweel (2000). For the current work the in-depth error analysis of the PIV system was not undertaken. Instead a simple estimation of ±0.1pixel accuracy for the two-dimensional PIV techniques was deemed sufficient to validate the results. The application of Stereoscopic PIV is essentially the application of two standard two-dimensional PIV systems that when combined together produce a two-dimensional plane of all three components of velocity. To accurately resolve the third component the cameras are placed at significant angles to one another and the field of view, as mentioned previously. These angles produce a perspective in each view, so a calibration of the cameras is required to dewarp the images and remove the perspective. After the images are dewarped into the global frame they are then processed producing two two-dimensional vector fields which when combined, accounting for the camera view orientations, produce the three components of velocity discussed. The velocity components (U_x, U_y, and U_z) were computed using the stereoscopic cross-correlation of pairs of successive images with 50% overlap between the interrogation domains. The images were processed using an advanced multi-pass method where the initial and final correlation passes were 32x32 pixels and 16x16 pixels, respectively. 250 image pairs were acquired to produce a time-averaged vector field for each plane. More information on the SPIV technique and vector calculation can be found in the LaVision manual (2007).

For the wind tunnel SPIV, the cameras and the laser optical head were each rigidly attached to a three axis Velmex Bi-Slide stepper motor controlled traversing system, which has a positional accuracy of ±4μm. This positioning system allowed for the cameras and the laser to be uniformly translated after the system was focused and calibrated, which enabled multiple streamwise data planes to be collected at incremental spanwise positions so that a full three dimensional time-averaged fluid volume could be reconstructed. The data collection and reconstruction method is discussed in more detail in the following sub-sections.

2.4.2.1 Volume Reconstruction

Data on multiple spanwise planes (1*mm* apart, see Figure 2.7) were acquired along the central region of the span (i.e., center jet in the middle module). Note that the solid lines in Figure 2.7 (on the right) represent the planes where data were acquired while the dashed lines are the symmetry planes (total of 25 planes). Stereoscopic PIV data collected on these planes were within a window size of about 25*mm* x 25*mm*. The data from all the planes were then reconstructed into a volume to provide the 3-D interaction domain between the synthetic jet and cross-flow.

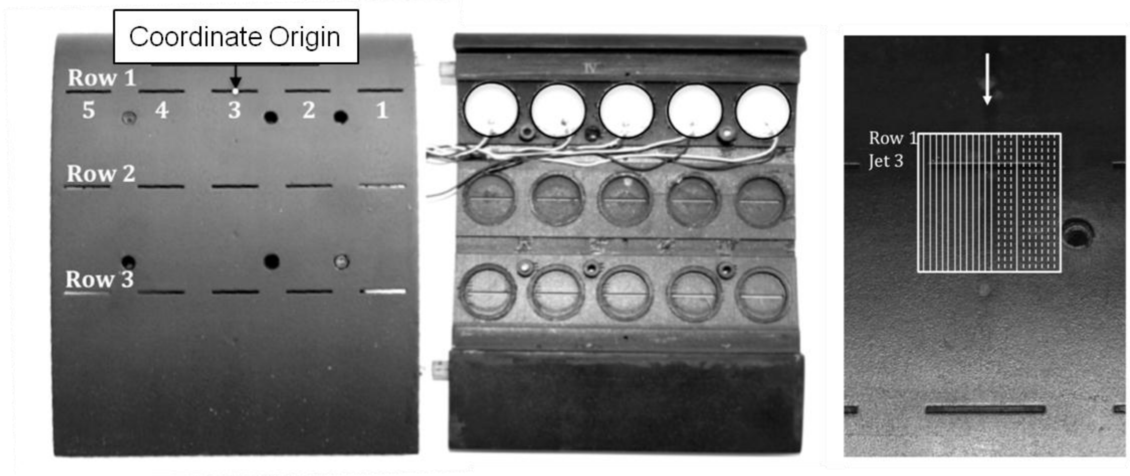

2.7: Picture of the center module, with three rows of jets and five jets in each row, front side (left) and backside (middle). On the right, PIV measurement planes at jet 3; solid lines represent planes on which data were acquired while dashed lines represent mirrored planes.

3. Results[2]

This section is divided into five sections, with section 3.1 displaying the global effects of separation and reattachment of the flow at various Reynolds numbers and angles of attack. Section 3.2 validates the mid-span quasi-two dimensional assumption made in the first section, where the formation of secondary flow structures is examined in sections 3.3.and 3.4, with the data being time averaged and phase averaged, respectively. Section 3.5 then studies the prevailing coherent and random motions throughout the flow field. The data focus first on a relatively large (55mm x 55mm) interrogation window to explore the effect of the Reynolds number and angle of attack and then a much smaller (25mm x 25mm) window is used for the remaining sections.

3.1 Reynolds Number and Angle of Attack Effect

First, the ability of the synthetic jets to modify the flow field around the wing was investigated at varying angles of attack and Reynolds numbers. This was done by collecting data for a range of angles (0^0 to 20^0) at three Reynolds numbers (50,000; 100,000; 250,000), at a blowing ratio of 1.2. The data were collected at the mid-span of the finite wing, far enough from the tip and root, where the flow is quasi two-dimensional and therefore has a negligible spanwise component. This allowed data to be collected using the less complex two-dimensional PIV.

Figure 3.1 and 3.2 present black and white contours of the normalized velocity for $\alpha = 10^0$ and 18^0, respectively, for each of the Reynolds numbers. Data were collected across jet 3 (see figure 2.7 above). At $\alpha = 10^0$ the effect of the Reynolds number is clearly visible; at the lowest Reynolds number tested (50,000, figure 3.1a), the flow is separated at x/c = 0.25 as is expected for this very low Reynolds number. Conversely, at a Reynolds number of 100,000 (figure 3.1b), the separation moves farther downstream, as expected from a thick airfoil. At the highest Reynolds number tested

[2] Portions of this chapter previously appeared as: Sahni, O., Wood, J., Jansen, K.E. & Amitay, M. (2011). Three Dimensional Interactions between a Finite-Span Synthetic Jet and a Cross-Flow. *Journal of Fluid Mechanics*, *671*, 254-287.

(250,000, figure 3.1c) the flow in the interrogation domain is fully attached. For the two lower Reynolds numbers cases, the effect of actuation is to reattach the separated flow. This can be expected to lead to a global increase in circulation, higher lift coefficients, and lower drag coefficients. At the Reynolds number of 250,000, where the baseline flow is already fully attached, and the effect of the actuation is to virtually modify the streamlines near the surface, where the near surface velocities are decreased, which although not a positive for maximum lift generation, can be advantageous for vehicle control.

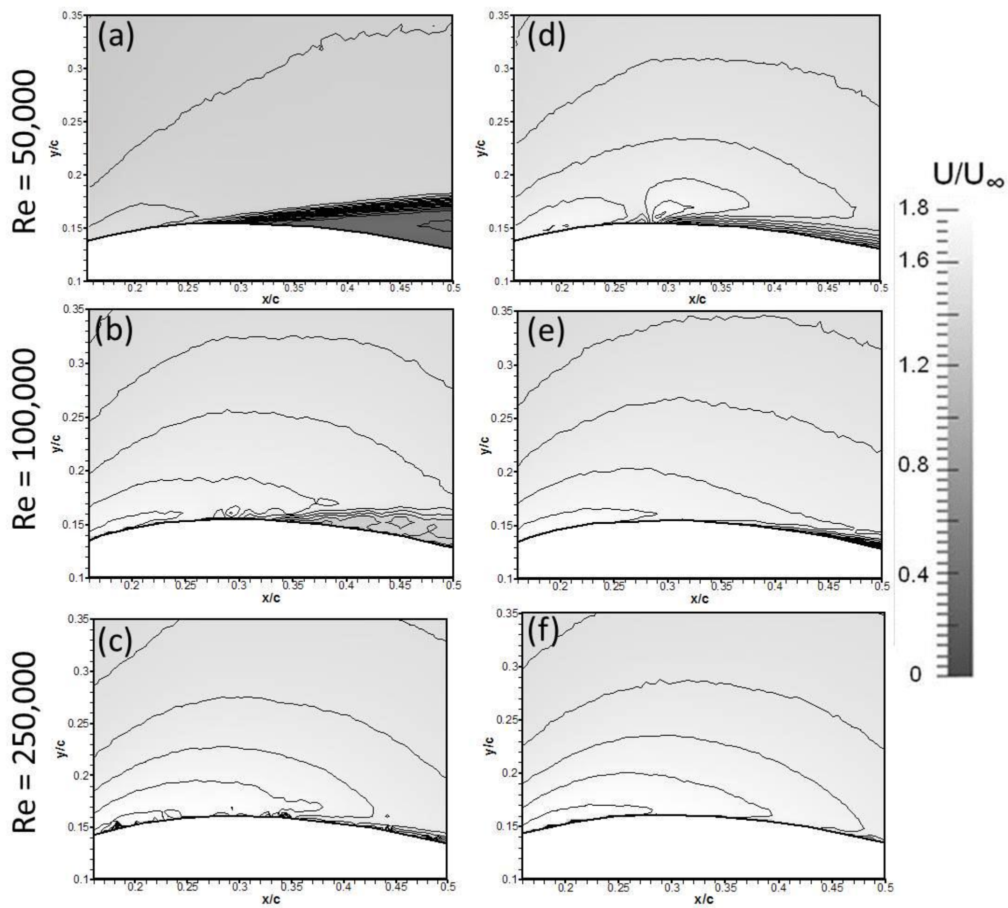

3.1: Total velocity data for baseline (a-c) and forced cases with C_b = 1.2 (d-f) at 10^0 angle of attack. Reynolds numbers of 50,000 (a, d), 100,000 (b,e), and 250,000 (c,f) are shown.

The normalized total velocity plots of the effect of Reynolds number at 18^0 angle of attack are shown in figure 3.2, where the baseline and the actuated cases are presented in figures 3.2a-c and 3.2d-f, respectively. All of the baselines at this angle are fully separated, and the sinusoidal actuation in all cases reattaches the flow, with slightly better effects seen at the higher Reynolds numbers. This result is due to the reduced viscous effects at the higher Reynolds numbers.

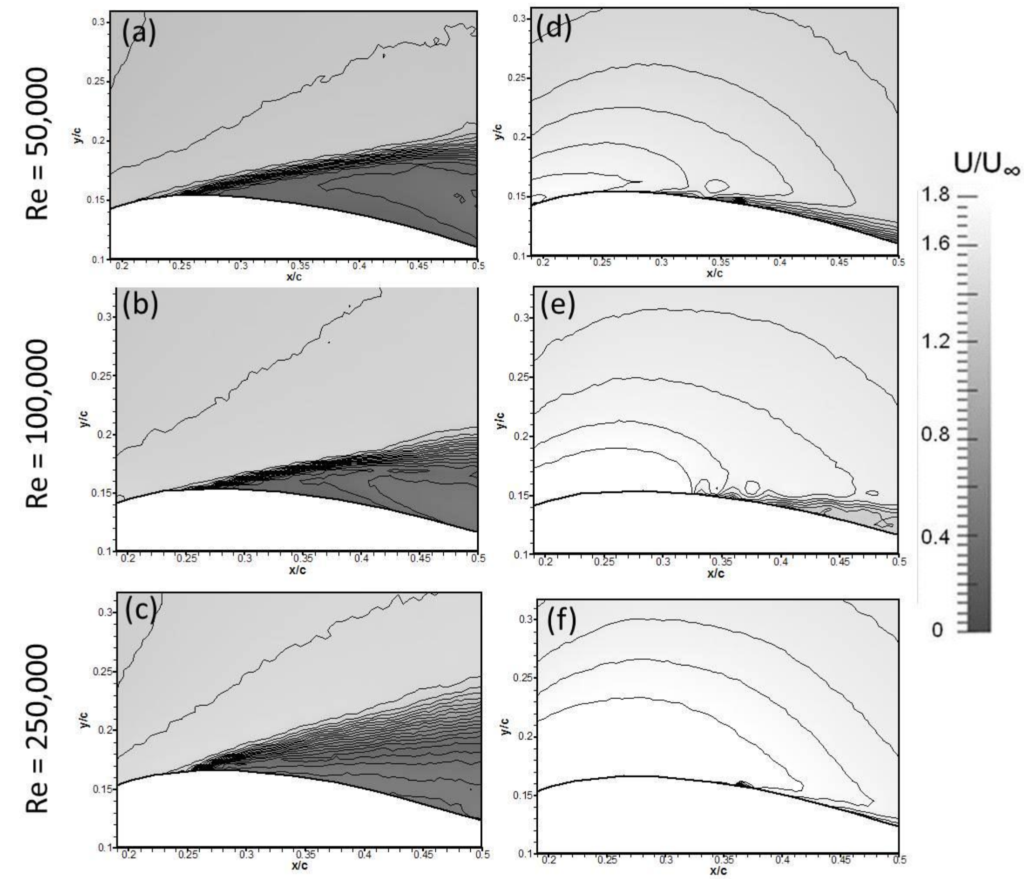

3.2: Total velocity data for baseline (a-c) and forced cases with C_b = 1.2 (d-f) at 18^0 angle of attack. Reynolds numbers of 50,000 (a, d), 100,000 (b,e), and 250,000 (c,f) are shown.

It can be seen from figures 3.1 and 3.2 that the jets are quite effective at reattaching the flow at varying angles of attack, when compared to the baseline cases. As a first step in understanding the effect of the synthetic jets, the interaction of a single synthetic jet with the cross flow at a chord Reynolds number of 100,000 and at an angle of attack of 0^o was investigated.

3.2 Quasi-Periodic Flow along the Mid-Span: Actuated Cases

To simplify the experimental efforts, an assumption was made that the baseline flow field over a portion (mid-section) of the finite wing is 2-D and the actuated flow is quasi-periodic along the span. However, no assumption was made regarding the interaction domain (between the synthetic jet and cross-flow), which, as will be shown later, is highly 3-D. These assumptions were verified experimentally and are presented in Figure 3.3. It is noteworthy to mention that Greenblatt & Washburn (2008) showed experimentally that the flow over a finite span wing with no sweep (with a similar aspect ratio as the present model) is quasi 2-D over a large portion of the span. To verify that the actuated flow field is quasi-periodic along the span (in the middle section), synthetic jets were activated at the highest blowing ratio of 1.2. The rational is that if the flow field for the highest blowing ratio is periodic then actuated cases with lower blowing ratios must be as well. Figure 3.3 presents contour plots of the actuated flow field in the vicinity of the synthetic jets, where data were acquired across the center-plane of jets 2, 3 and 4 (see notation in Figure 2.7). The figure shows time-averaged total velocity fields (Figures 3.3a-c) and phase-averaged spanwise vorticity fields (Figures 3.3d-f; at a phase of $\phi = 240^0$ during the synthetic jet driving cycle; where the start of the jet cycle ($\phi = 0^0$) is considered at the beginning of the blowing portion of the cycle. Note that the phase is measured with respect to the driving signal and not the velocity output of the slot, which is about 30^o off. This phase difference suggests that compressibility effects are present (Gallas et. al., 2003). Furthermore, in the phase-averaged vorticity plots the background color is set to zero value, implying that lighter shades (than the background color) indicate clockwise (CW) vorticity whereas darker shade represent counter-clockwise (CCW) vorticity. The velocity, as well as the vorticity, fields at the three planes show similar flow structures from three different jets in the mid-span and thus, justifying the assumption made above. Therefore, the focus is placed on the center jet (jet 3 in Figure 2), and a detailed discussion on the velocity and vorticity fields, based on both experimental and numerical data, is presented in subsequent figures and subsections.

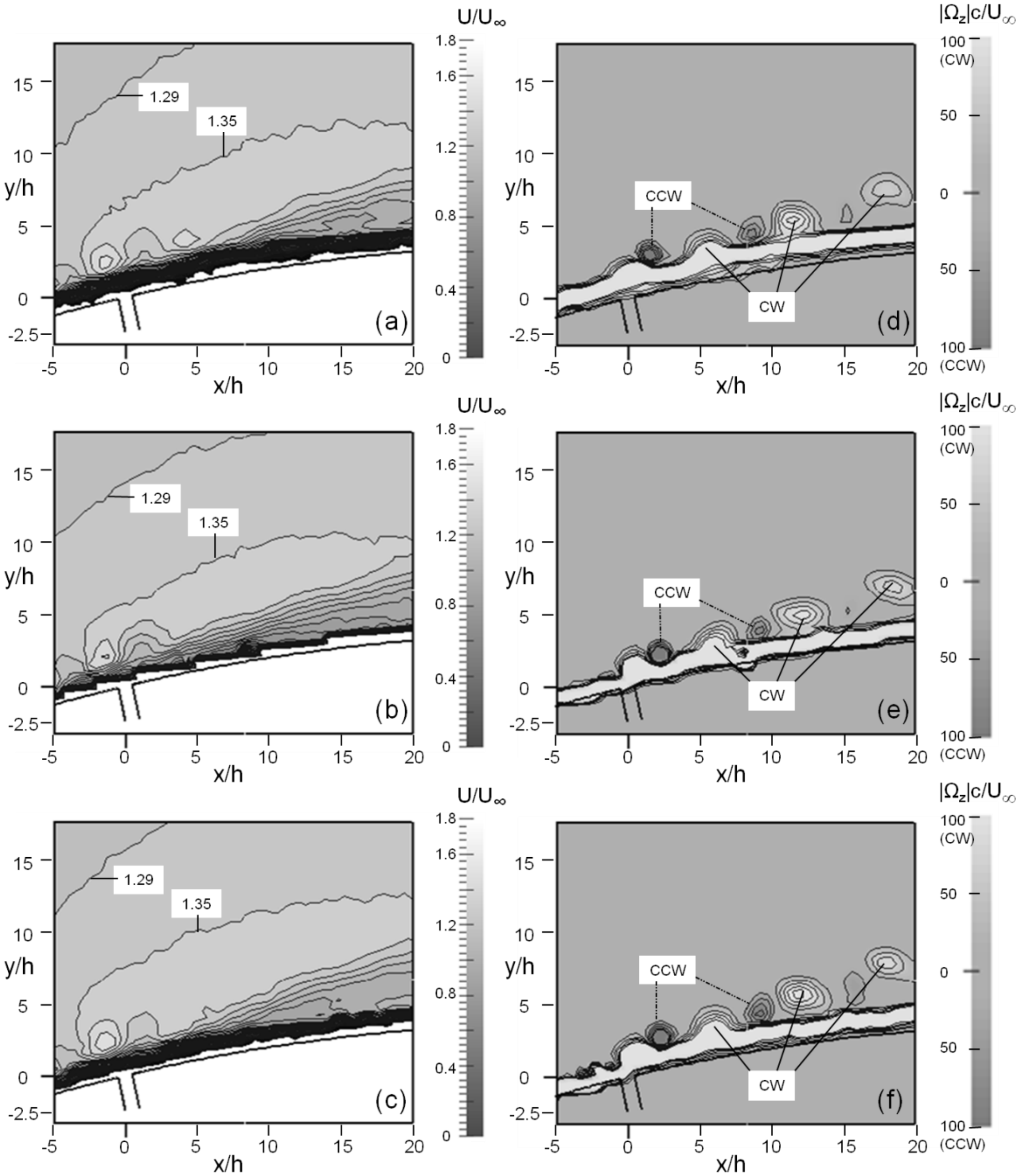

3.3: Experimental data of time-averaged total velocity (a-c) and phase-averaged spanwise vorticity (d-f) fields across the center-plane of jets 2 (a, d), 3 (b, e), and 4 (c,f).

3.3 Time-Averaged Flow Field

A quantitative comparison between the experimental and numerical results is obtained by showing line plots at different chordwise locations, as presented in Figure 3.4. Note that the location of each line plot is presented at the top of Figure 3.4 (where five streamwise locations are considered). A contour plot of the baseline total velocity across the center-plane of jet 3 is presented in Figure 3.4; this interrogation domain, in the vicinity of the jet, is selected to enable detailed study of flow structures and interactions due to actuation. The lines are normal to the surface and include downstream as well as upstream locations very near to the jet orifice. The distance normal to the surface (referred to as y_n) is normalized by h (the width of the synthetic jet orifice) for comparison with the forced cases that follow. Velocity profiles on subsequent lines are offset by a unit distance of $U/U_\infty = 1$. Note that the experimental data (symbols) are plotted from a distance h away from the surface (i.e., from $y_n/h = 1.0$) due to the limitations of the PIV measurements very near to a solid curved surface (i.e., within 0.75*mm*).

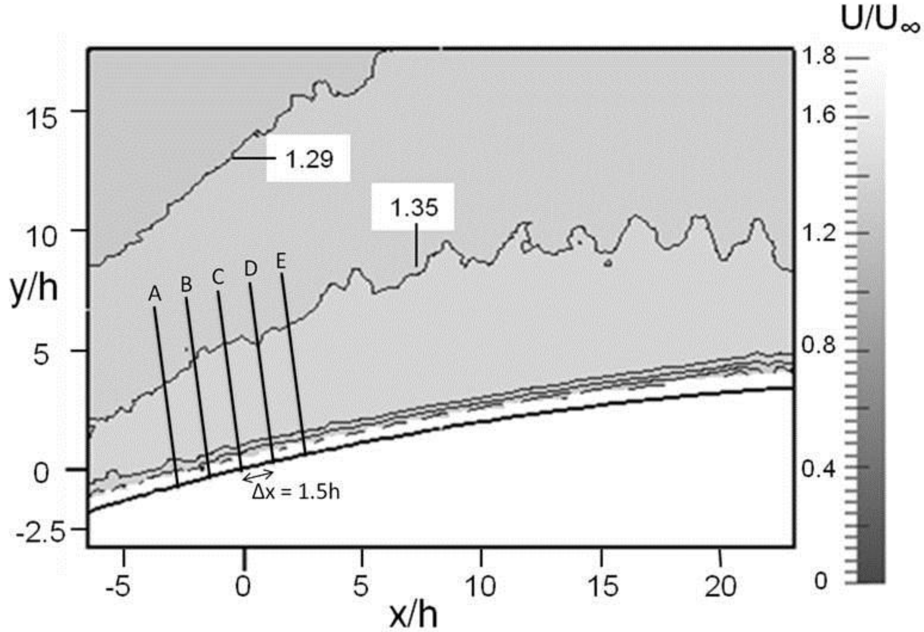

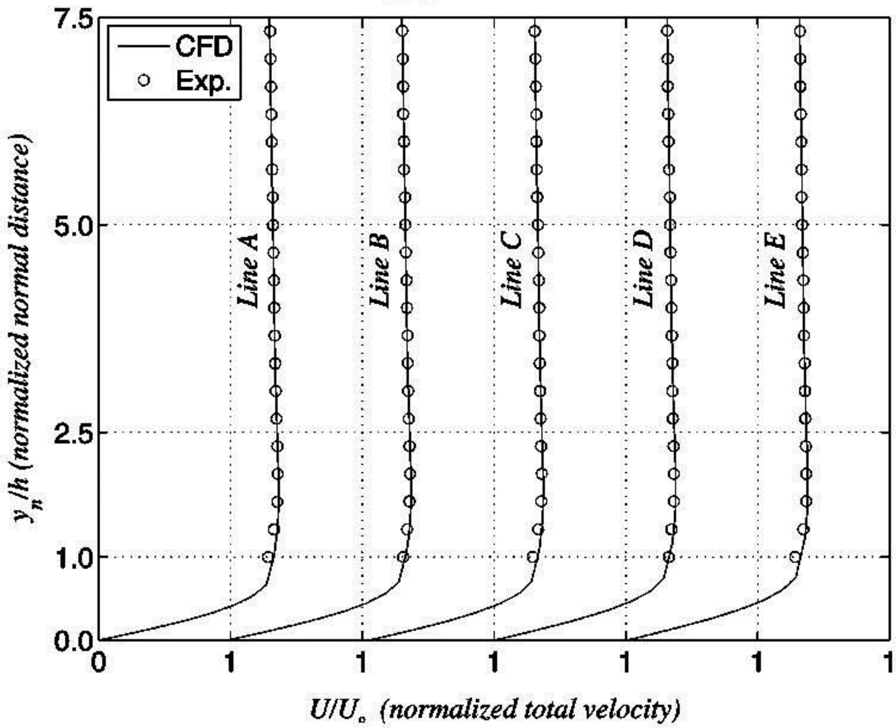

3.4: Contour plot of the total velocity across the center-plane of jet 3; time-averaged total velocity profiles along five lines normal to the surface at x/h = -3 (line A), -1.5 (line B), 0 (line C at jet exit), 1.5 (line D), and 3 (line E). Velocity profile on subsequent lines are offset by a unit distance of U/U_∞ = 1

Next, the time-averaged interaction between the synthetic jet and cross-flow is presented in Figures 3.5 and 3.6, using the same interrogation domain as the baseline case, where the experimental measurements are compared to the numerical results. Two actuated cases are examined here: $C_{\mu c2}$ and $C_{\mu c6}$ (corresponding to blowing ratios of C_b = 0.4 and C_b = 1.2, respectively). Figure 3.5 presents contour plots of the total velocity across the center-plane of jet 3, where the experimental results are shown in Figures 7a and b while the numerical results are displayed in Figures 7c and d. The forcing levels corresponding to C_b = 0.4 and C_b = 1.2 are presented in Figures 7a and c, and Figures 7b and d, respectively. The introduction of the synthetic jet into the cross-flow yields three primary effects on the mean flow (compared to the baseline flow field): (1) reduced velocity just upstream of the jet, (2) higher velocity downstream of the jet, and (3) thickening of the boundary layer downstream of the jet. These effects are much more pronounced for the case with a higher blowing ratio.

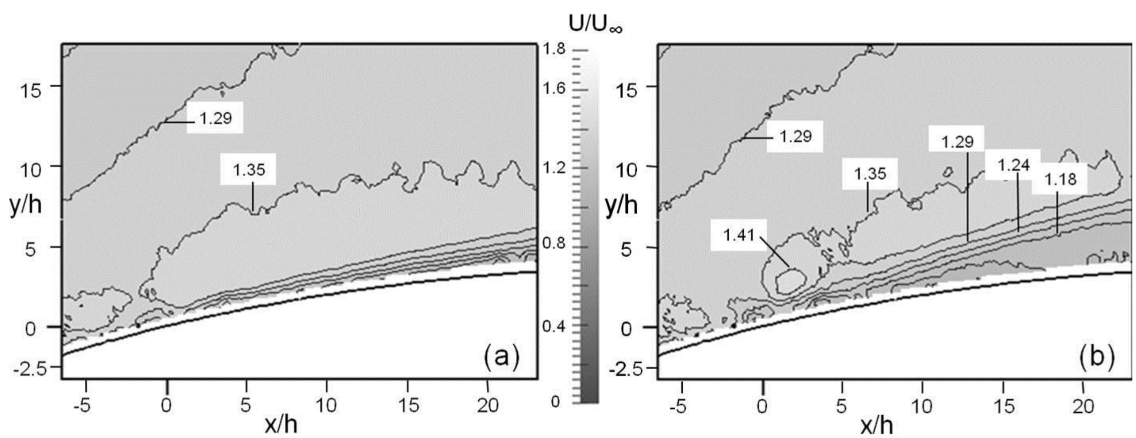

3.5: Contour plots of the total velocity across the center-plane of jet 3; Forced cases with C_b = 0.4 (a) and 1.2 (b).

The effect of the synthetic jet on the velocity field was also examined using line plots at the same locations as in the baseline case (discussed in Figure 3.4). Figure 3.6 shows the total velocity profiles along the same five lines used in Figure 3.4, for C_b = 0.4 (Figure 3.6a) and C_b = 1.2 (Figure 3.6b). The velocity profiles on subsequent lines are offset by a unit distance of $U/U_\infty = 1$. The plots include the experimental measurements (symbols) and simulation results (lines). These plots show that as the blowing ratio increases the effect of the synthetic jet is felt farther away from the wall and a velocity maximum in the velocity profile is obtained downstream of the jet. In a measurement window with such a strong velocity gradient uncertainty in PIV increases significantly, specifically for the maximum jet speed (see Yao et. al., 2004).

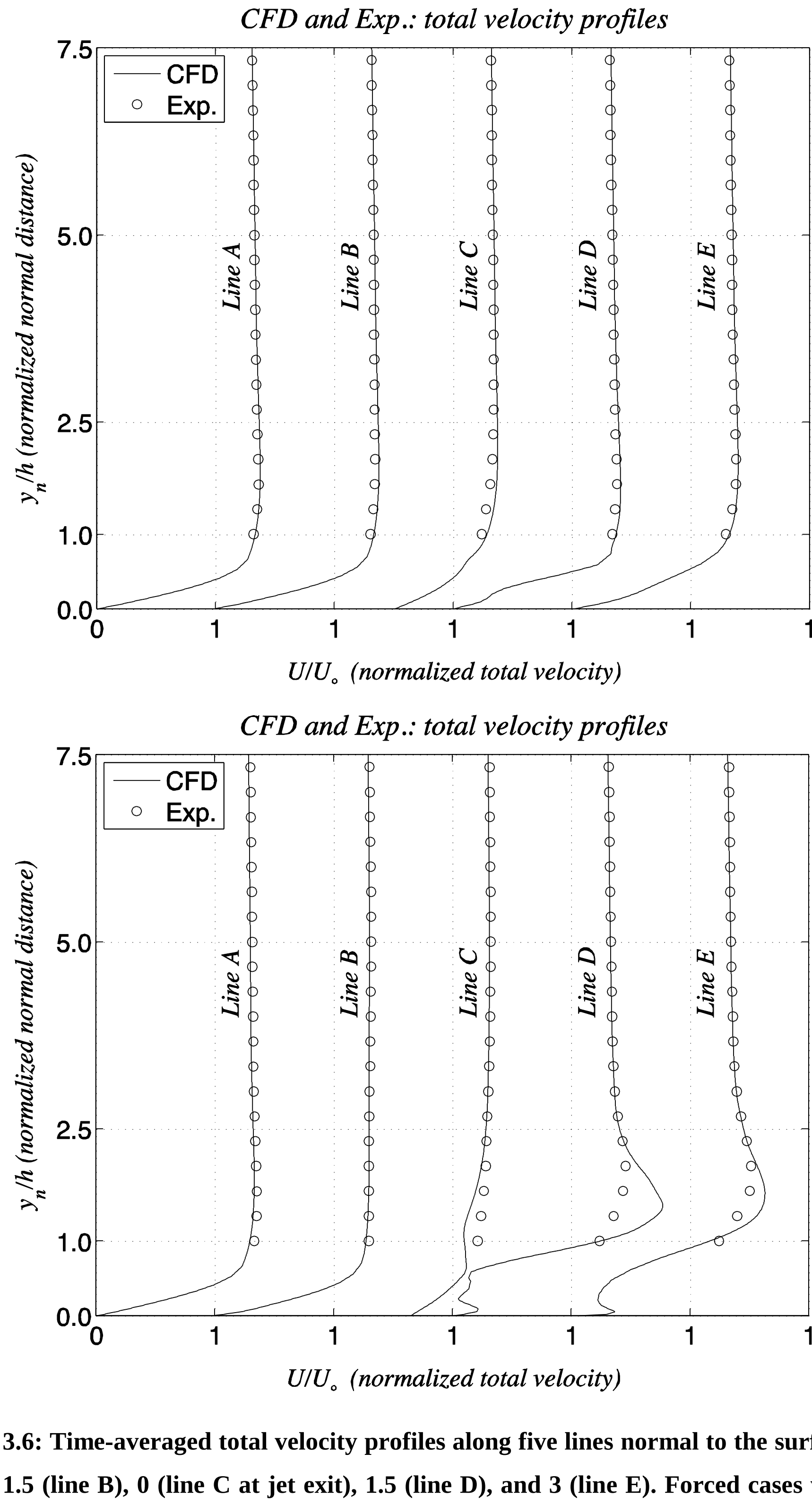

3.6: Time-averaged total velocity profiles along five lines normal to the surface at x/h = -3 (line A), -1.5 (line B), 0 (line C at jet exit), 1.5 (line D), and 3 (line E). Forced cases with C_b = 0.4 (a) and 1.2 (b).

Due to the finite-span of the synthetic jet the interaction between the jet and cross-flow is expected to be 3-D. Therefore, time-averaged iso-total velocity surfaces, based on the volumetric data over a spanwise strip of $z/h = 32$, were calculated and are presented in Figure 3.7. The spanwise extent of this interrogation domain was selected such that it is centered at the mid-span of jet 3 and extends $L_z/4$ (quarter span of the jet slit) from the edge of the slit on each side (see Figure 2). Furthermore, in Figure 9 the effects of the blowing ratio on the flow interaction, and the formation of the secondary flow structures, were also explored. Six levels of blowing ratios, i.e., $C_b = 0.2, 0.4, 0.6, 0.8, 1.0$, and 1.2, that were considered experimentally are shown in Figures 9a-f, respectively, where an iso-total velocity surface is shown at a level of $U/U_\infty = 1.3$. For all blowing ratios, the interaction domain consists of secondary flow structures. Furthermore, as C_b increases the interaction domain is affected as follows: (1) the penetration of the jet into the cross-flow is increased, (2) three-dimensionalities begin to appear closer to the slit, (3) the spanwise wavelength of the secondary structures in the mean flow increases, and (4) the spanwise extent of the interaction domain decreases. The trends of (1) and (2) are expected as the jet becomes stronger in the cross-flow, where mid-range cases (with $C_b = 0.6$ and $C_b = 0.8$) exhibit combined features from the low blowing ratio range (with $C_b = 0.2$ and $C_b = 0.4$) as well as from the high blowing ratio range (with $C_b = 1.0$ and $C_b = 1.2$); namely, in the mid blowing ratio range flow structures are 2-D very near the slit, similar to the low-range, but they merge and lift-off at downstream locations, similar to the high-range. On the other hand, it is noteworthy to mention that the trends of (3) and (4) are similar to what was shown by Amitay & Cannelle (2006) for a finite-span synthetic jet issued into a quiescent flow (in their work, the strength of the synthetic jet was determined using the stroke length, L_0, due to the absence of a free-stream). Moreover, Amitay & Cannelle (2006) showed that the strength of the secondary flow structures and their spanwise wavelength also vary with the aspect ratio of the synthetic jet slit.

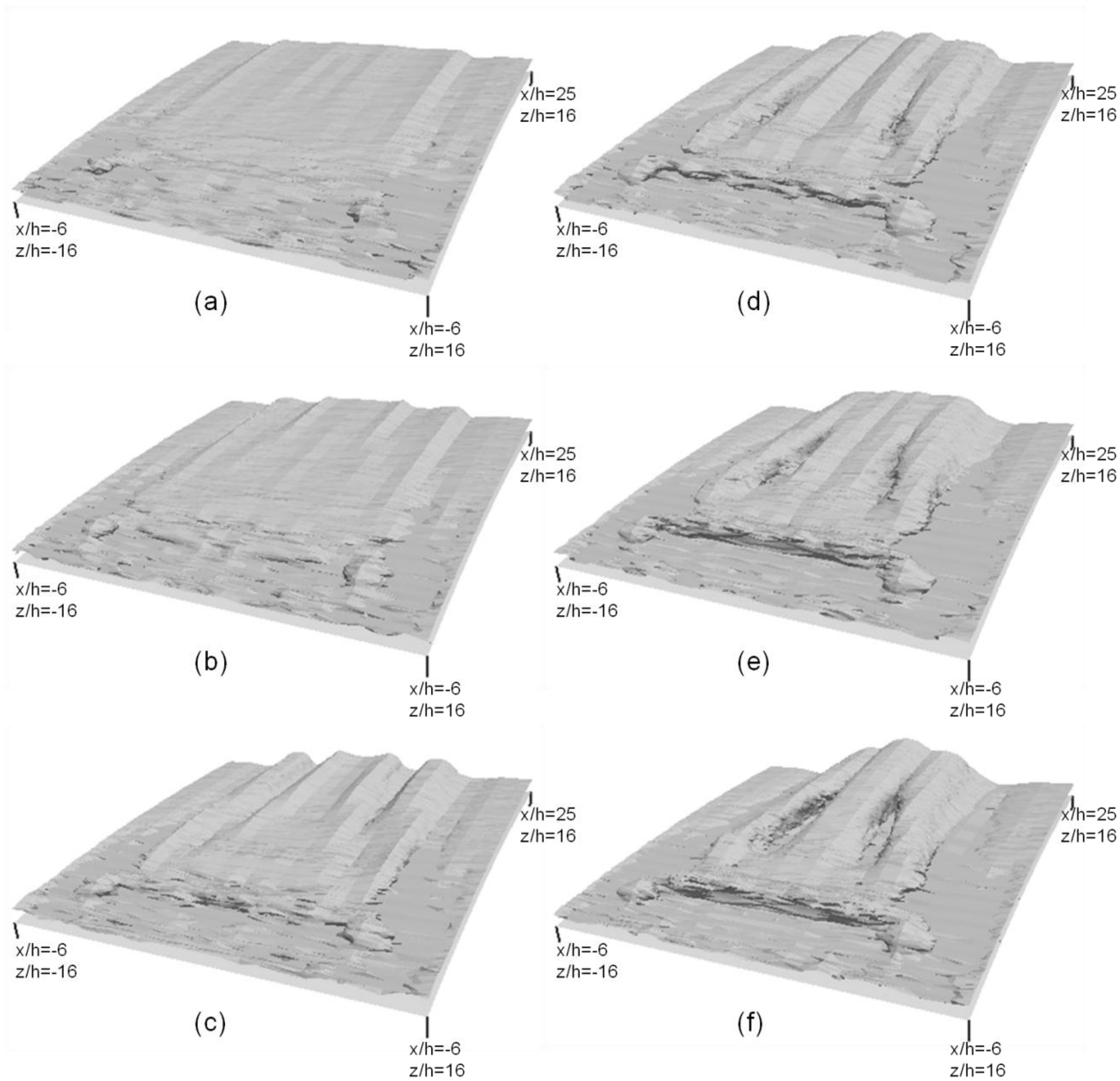

3.7: Effect of the momentum coefficient on the time-averaged (volumetric) flow field; experimental data for six actuated cases; C_b = 0.2 (a), 0.4 (b), 0.6 (c), 0.8 (d), 1.0 (e), and 1.2 (f). Iso-surface of total velocity at U/U_∞ = 1.3.

Furthermore, in the C_b = 0.4 case multiple small and organized streamwise-oriented secondary structures are formed in the mean flow; however, due to the limited spatial-resolution of PIV measurements these small structures are not well captured in the experimental data. This small-amplitude waviness in the distribution corresponds to the development of secondary streamwise vortical structures. These secondary flow structures are organized in a symmetric fashion about the center-plane of the jet. In the high blowing ratio case with C_b = 1.2 these structures are much larger both in the wall-normal and spanwise (larger wavelength) directions. Furthermore, they appear to be merged together, namely, with a lobe in the middle and a lobe near each end (also note that these structures develop immediately downstream of the slit, unlike the low blowing ratio case). It is noteworthy to mention that these secondary flow structures are formed due to the finite-span of the synthetic jet and can play an important role in various flow control applications (e.g., separation control, virtual aero-shaping, etc.).

3.4 Phase-Averaged Flow Field

In order to fully understand the formation and evolution of the secondary flow structures one also needs to examine the instantaneous and the phase-locked flow fields. Therefore, Figures 3.8–3.12 present phase-averaged span-wise vorticity based on experimental results, while Figures 3.13 presents instantaneous span-wise vorticity based on numerical results. Terms clockwise (CW) and counter-clockwise (CCW) are used to define the direction of the span-wise vorticity. Note that vorticity due to the cross-flow boundary layer is in the clockwise direction.

Figures 3.8–3.11 display the experimental results of the phase-averaged span-wise vorticity. Figures 3.8 and 3.9 present data at the center-plane for two actuated cases with C_b = 0.4 and C_b = 1.2, respectively, whereas Figures 3.10 and 3.11 provide volumetric view of the same two actuated cases in terms of iso-vorticity surfaces. These figures include two phases of ϕ = 120^0 and ϕ = 240^0 in the synthetic jet cycle.

Figure 3.8 presents the actuated case with C_b = 0.4. The evolution of periodic vortical structures issued by the synthetic jet can be clearly seen in this interrogation window. Note that the counter-clockwise (CCW) vorticity (associated with the synthetic jet) is absent in this case (outside of the jet slot) as it is not strong enough to overcome the CW vorticity of the cross-flow boundary layer. However, the periodic nature of the synthetic jet leads to a train of coherent (clockwise) vortices in the boundary layer that advects downstream with the main flow. Each vortex undulation corresponds to actuation caused in a synthetic jet cycle. At a phase of 120^0 the vortical structure formed in the current jet cycle exists very close to the orifice (Figure 3.8a), whereas by the phase of 240^0 it is advected downstream, as shown in Figure 3.8b. Furthermore, since here C_b = 0.4, (i.e., a weak jet) the vortical flow structures stay close to the surface.

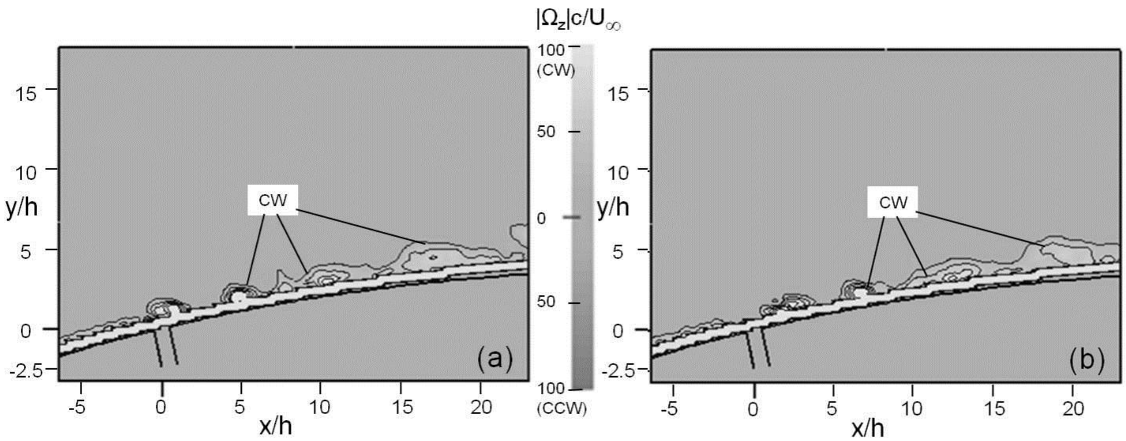

3.8: Center-plane phase-averaged span-wise vorticity for an actuated case with C_b = 0.4 at two phases; ϕ = 120^0 (a) and 240^0 (b). Lighter shade is used for CW vorticity while darker for CCW vorticity.

Figure 3.8 shows phase-averaged span-wise vorticity for the case where the synthetic jet is activated at a higher blowing ratio of C_b = 1.2. In this case, in contrast to the low blowing ratio case, both CW and CCW vortices are present, and furthermore, vortical structures are distinctly bigger than the lower blowing ratio case and penetrate much deeper into the main flow and eventually lift-off the surface. At the phase of 120^0 (Figures 3.8a), vortical structure issued from the jet orifice in the current cycle can be clearly seen just downstream of the jet slit. However in contrast to the low blowing ratio case, a discrete counter-rotating vortex pair exists and is tilted due to the cross-flow. At a later phase of 240^0 (Figures 3.8b), the CCW vortex appears to roll over the CW vortex in the pair and resides in between two CW vortices issued in subsequent synthetic jet cycles. The reason for this is because CCW vortex experiences higher cross-flow velocity during the jet cycle while it advects through a region outside of the cross-flow boundary layer. This behavior leads to a train of counter-rotating vortices with diminishing strength that eventually lifts off the airfoil surface. As will be shown in

Figure 3.12 below, the CCW vortices of the synthetic jet are responsible for the lift-off mechanism.

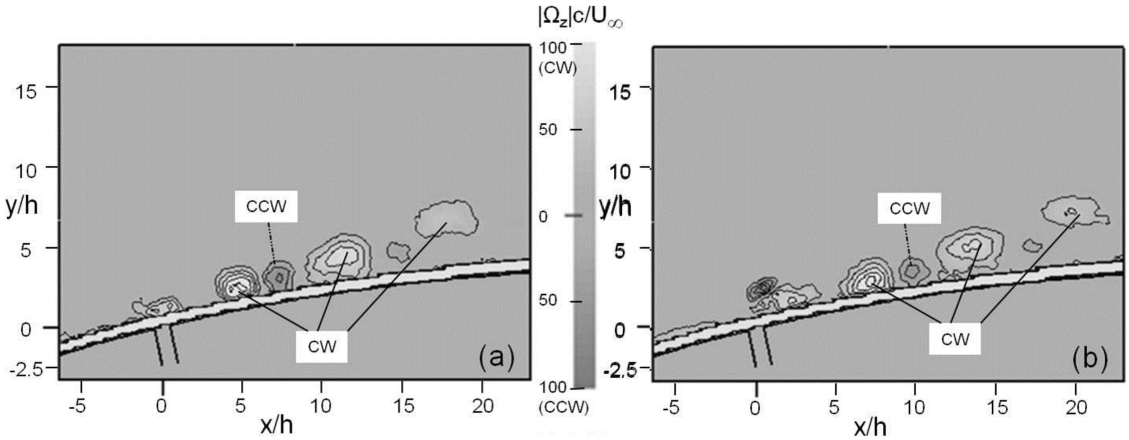

3.9: Center-plane phase-averaged spanwise vorticity for an actuated case with C_b = 1.2 at two phases; ϕ = 120^0 (a) and 240^0 (b). Shades are same as in Figure 3.8.

Due to the 3-D nature of the interaction between the synthetic jet and cross-flow, one needs to measure the 3-D flow field. Figures 3.10 and 3.11 present iso-surfaces of phase-averaged spanwise vorticity, based on experimental and numerical results, for C_b = 0.4 and C_b = 1.2, respectively. Two levels of spanwise vorticity are considered, which are equal in value but opposite in directional sense, i.e., one is CW while the other is CCW. The non-dimensional value for these iso-surfaces is set to $|\Omega_z|c/U_\infty$ = 30.5.

Figure 3.10 shows the phase-averaged flow field at ϕ = 120^0 and ϕ = 240^0 for the low blowing ratio case (C_b = 0.4). As can be seen, spanwise rollers, issued by the finite-span synthetic jet, are dominated by the clockwise structures near the jet slit. At downstream locations, organized secondary structures evolve, but the experimental data captures the trend with limited spatial resolution along the span due to the spacing between PIV planes. For this low blowing ratio case, the first two roller structures (issued in two subsequent synthetic jet cycles) are quasi 2-D, except near the edges of the slit where secondary structures form and perturb the rollers leading to the formation of 3-D flow structures farther downstream. It is due to these flow structures and interactions that small waviness or streak-like pattern is observed in the mean flow for the low blowing ratio case.

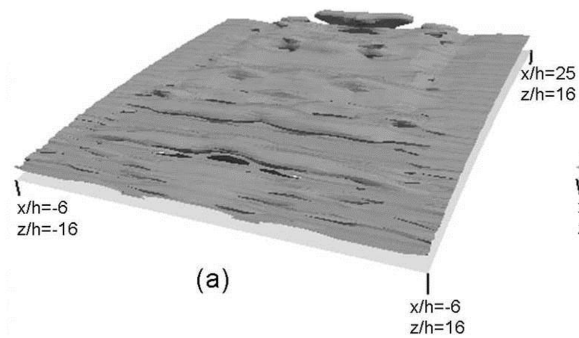

3.10: Iso-surfaces of phase-averaged spanwise vorticity $|\Omega_z|c/ U_\infty$ = 30.5; one in clockwise sense (in light shade) and other in counter-clockwise sense (in dark shade). For an actuated case with C_b = 0.4 at two phases; ϕ = 120^0 (a) and 240^0 (b).

Next, Figure 3.11 presents iso-surfaces of phase-averaged spanwise vorticity for the high blowing ratio case (C_b = 1.2). In this case, the spanwise rollers are distinctly bigger and CCW vortex structure is present. One can see that these coherent vortical structures lose two-dimensionality, lift-off the surface and possess less spanwise extent. All these observations are in accord with the ones discussed above.

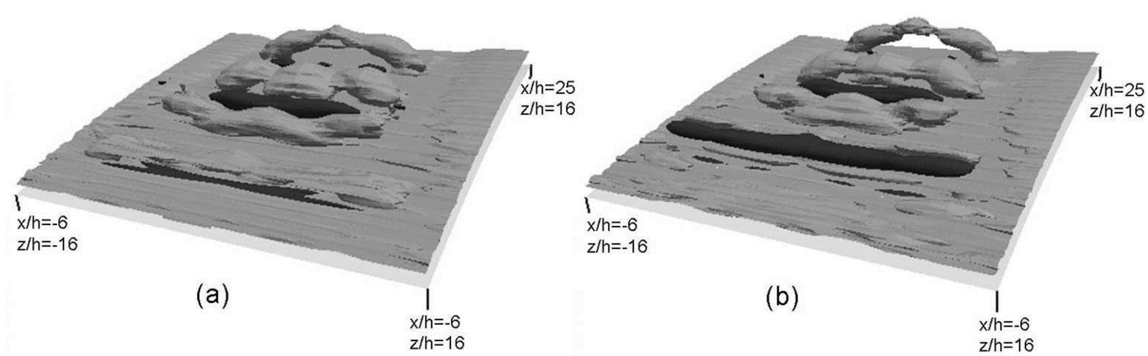

3.11: Iso-surfaces of phase-averaged spanwise vorticity $|\Omega_z|c/ U_\infty$ = 30.5; one in clockwise sense (in light shade) and other in counter-clockwise sense (in dark shade). For an actuated case with C_b = 1.2 at two phases; ϕ = 120^0 (a) and 240^0 (b).

To further understand the dynamics of vortical structures and their variation with the blowing ratio, experimental results are presented in Figure 3.12 for three different levels of blowing ratios; C_b = 0.4 (in the low level range), C_b = 0.8 (in the mid level range) and C_b = 1.2 (in the high level range). The figure presents phase-averaged spanwise vorticity across the center-plane of the jet at six different phases starting at the phase of 180^0; this choice was made because the counter-rotating vortex pair formed in the current cycle is clearly evident at the jet slit. Grid lines are included in this figure to provide the location of the vortical structures at different phases. For the low blowing ratio case (Figures 3.12a-f) the CW vorticity dominates, as the CCW vorticity portion of the synthetic jet is not able to overcome the CW vorticity of the cross-flow boundary layer. Thus, periodic excitation due to the synthetic jet leads to a wave-like undulation in the cross-flow boundary layer that is advected downstream with the main flow. As the blowing ratio is increased to C_b = 0.8 (Figures 3.12g-l), the CCW vortex is visible near the synthetic jet orifice; vortical structure issued by the synthetic jet can be seen at the phase of 180^0 (when counter-rotating vortical structure is clearly seen at x/h = 0, Figure 3.12g). In subsequent phase of 240^0 shown in Figure 3.12h, the current vortical structure issued by the synthetic jet is tilted due to the cross-flow. At this phase the CW vortical structure (immediately downstream of the orifice) remains near the surface while the CCW vortex rolls over it. In the next phase of 300^0 (Figure 3.12i) the CCW vortex collides with the CW structure and splits it, and then resides between the two segments of the split CW structure. Note that at the phase of 0^0 the front segment of the split CW structure is located at x/h = 5. By the phase of 60^0 this segment is completely diffused while the lagging segment distinctly exists just before x/h = 5. Moreover, the CCW vortex becomes weaker, as can be seen in phases of 120^0 and 180^0 (i.e., in between x/h = 5 and x/h = 10). This cycle continues and the lagging segment of CW vortical structure spreads and losses its coherence as it is advected downstream.

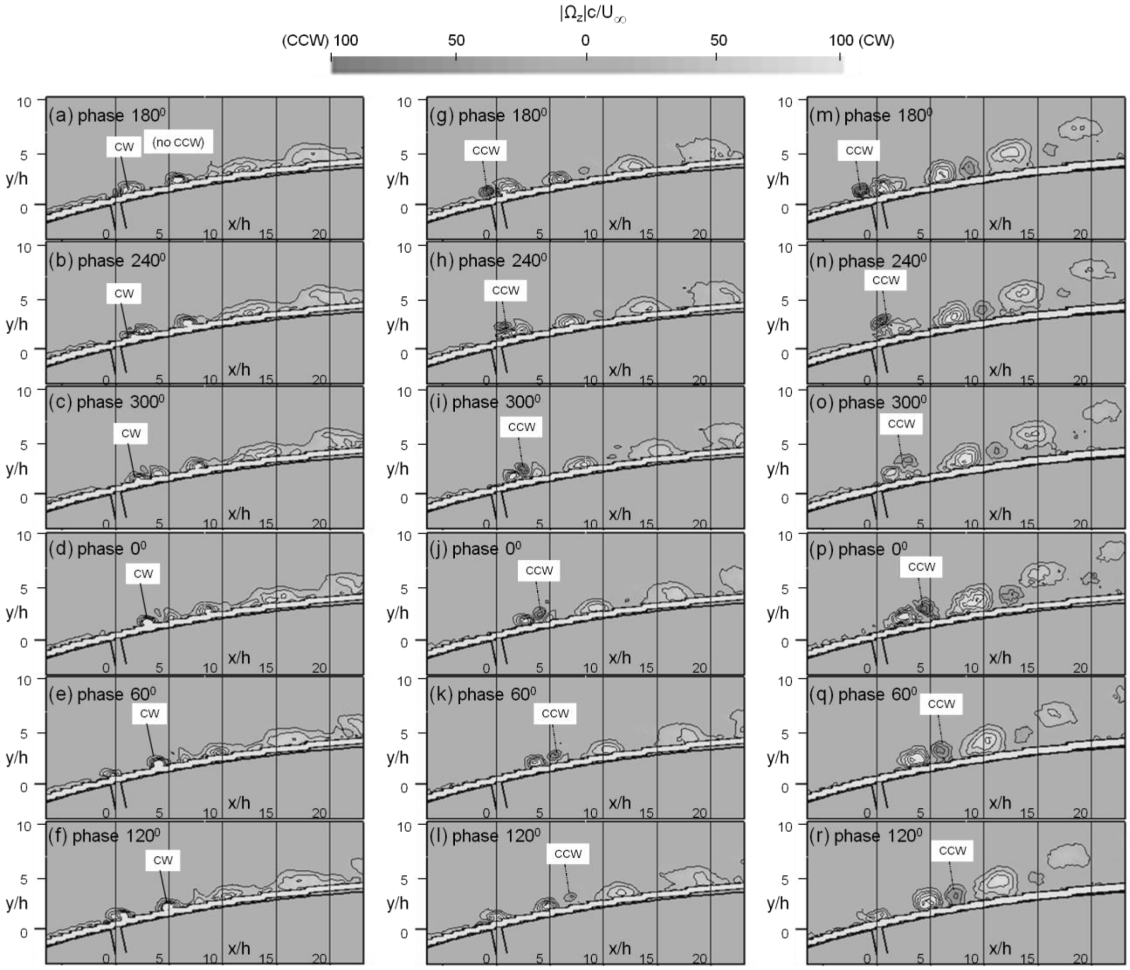

3.12: Phase-averaged spanwise vorticity based on experimental data on center-plane for three actuated cases with C_b = 0.4 (a-f), 0.8 (g-l), and 1.2 (m-r). Six different phases (at every 60^0 starting from 180^0 at the top most row) are considered to show temporal evolution and interactions of vortical structures.

Figures 3.12m-r show the evolution and advection of the vortical structures for the highest blowing ratio considered in this study (C_b = 1.2). At this blowing ratio, a counter-rotating vortex pair is issued from the jet orifice, which is titled by the cross-flow (see phase of 240^0, Figure 17n). In the next phase of 300^0 the CCW structure overtakes the CW as it experiences higher cross-flow velocity and resides between subsequent CW structures. Furthermore, by the next jet cycle the CCW structure due to its local upwash causes the downstream CW structure to lift-off the surface, e.g., at the phase of 300^0 in Figure 3.12o the CW structure from the previous cycle is lifted-off (at x/h = 15).

In general, the flow field can be decomposed into three components: mean (time-averaged) flow, coherent (phase-locked) structures, and turbulent (random) motions. To understand the importance of the coherent and random motions for different blowing ratios, instantaneous and phase-averaged spanwise vorticity fields were collected numerically (all numerical data courtesy of Sahni and Jansen of the Scientific Computation Research Center at RPI) and are compared in Figures 3.13 and 3.14. Figure 3.13 shows data across the center-plane of the jet whereas Figure 3.14 presents the volumetric view in terms of iso-surfaces. In these figures, numerical data is presented for two actuated cases with C_b = 0.4 and C_b = 1.2. For the low blowing ratio case, the vortical structures observed in the instantaneous and phase-averaged flow fields (Figures 3.13a and c, respectively) are nearly identical. For the higher blowing ratio case (C_b = 1.2), the situation is drastically different as the instantaneous field shows the presence of less coherent, turbulent motions whereas phase-averaged field, based on jet cycle, exhibits coherent structures issued by the synthetic jet. Note that for the low blowing ratio case the synthetic jet is laminar while for the high blowing ratio case the jet falls within the turbulent regime, as was described (using flow visualization) by Chen et. al. (2000).

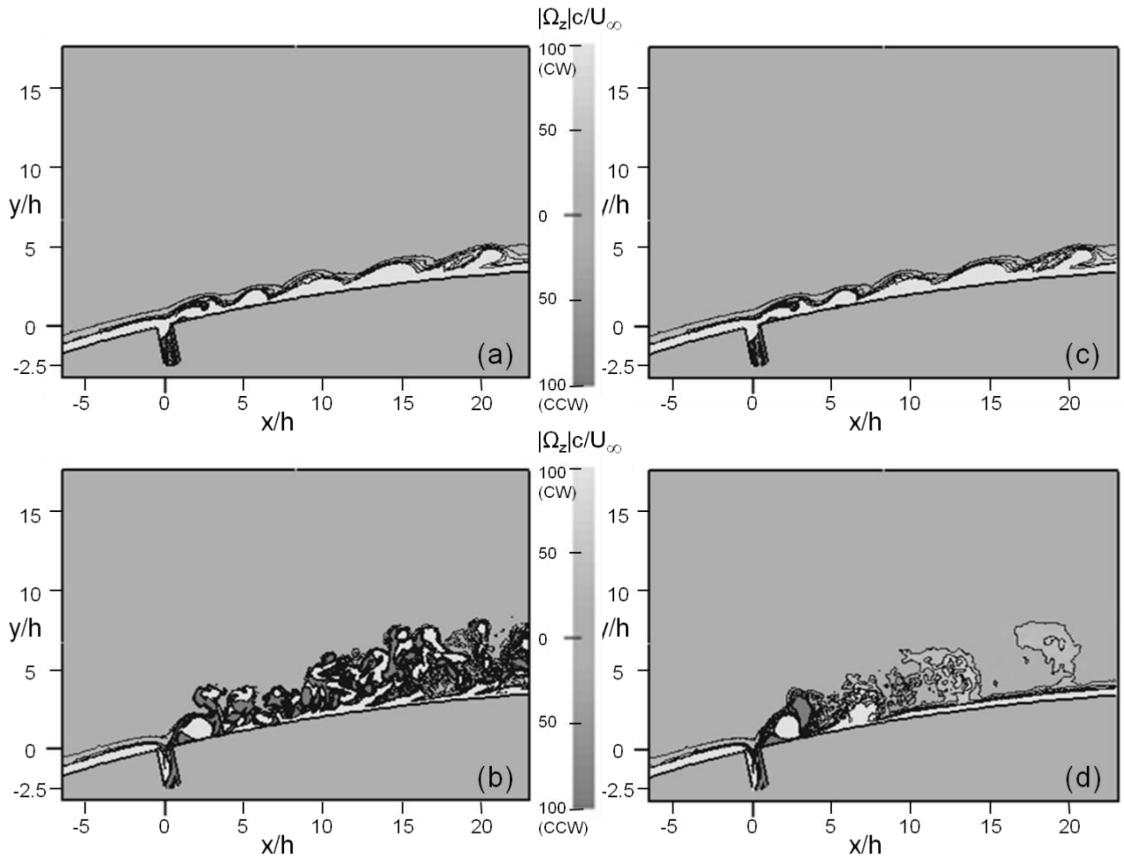

3.13: Spanwise vorticity, instantaneous (a,b) and phase-averaged (c,d), based on numerical data at center-plane for two actuated cases with C_b = 0.4 (a,c) and 1.2 (b,d) at a phase of 240^0. Shades are same as in Figure 13. Courtesy of Sahni and Jansen.

Finally, Figure 3.14 presents numerical data of the iso-surfaces of spanwise vorticity for the same two actuated cases at two phases of 120^0 and 240^0. In each plot, instantaneous and phase-averaged fields are presented in the left- and right-halves of the span, respectively (lines in the mid-span depict the center-plane). As before, the case with C_b = 0.4 (Figures 20a and c) shows nearly identical structures in the instantaneous and phase-averaged fields. Moreover, well-organized secondary structures are present. When the blowing ratio is increased to C_b = 1.2 (Figure 20b and d), turbulent motions are dominant in the flow. It is because of the presence of such turbulent motions that the mean flow exhibits structures that appear to be merged together (as shown in Figures 10b and d based on an iso-total velocity surface).

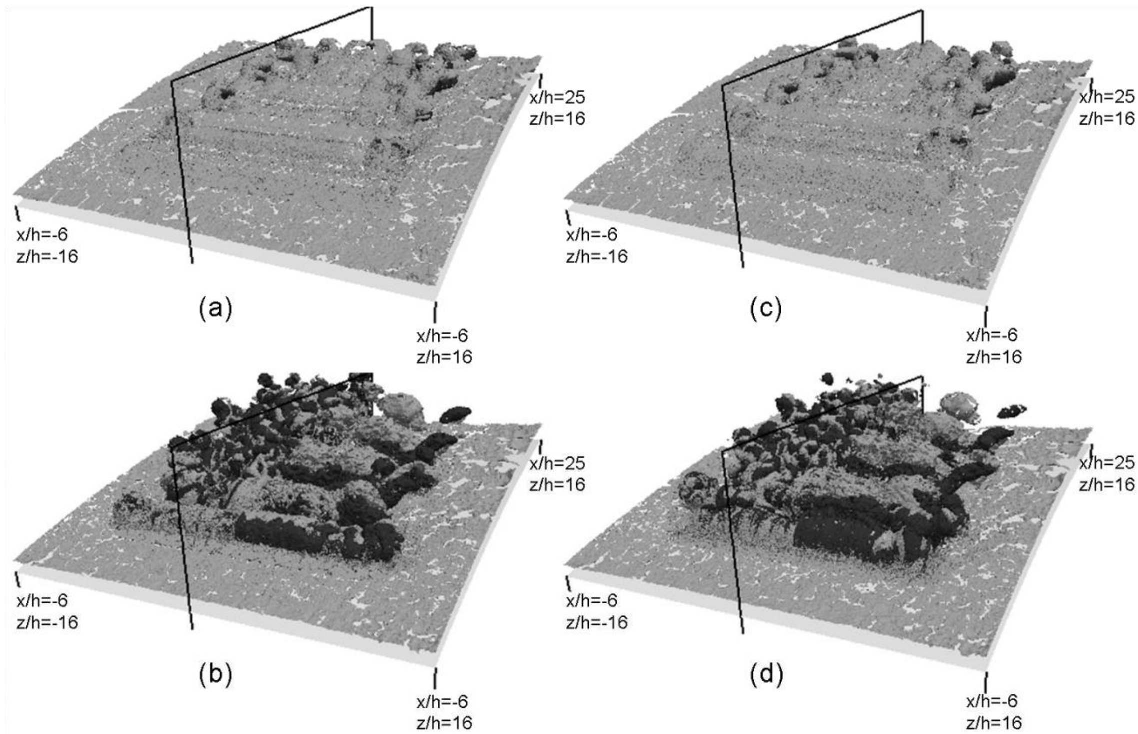

3.14: Iso-surfaces of spanwise vorticity, instantaneous (left-half of span in each case) and phase-averaged (right-half of span), with equal but opposite values of $|\Omega_z|c/ U_\infty$ = 30.5 (light shade is used for CW vorticity and dark shade for CCW). Numerical data is shown for two actuated cases with C_b = 0.4 (a, c) and 1.2 (b, d) at two phases; ϕ = 120^0 (a, b) and 240^0 (c, d). Lines in the mid-span depict the center-plane. Courtesy of Sahni and Jansen.

3.5 Triple Decomposition

The instantaneous data from the numerical simulation highlighted an import factor not yet explored: the coherent and random motions in the flow. In order to explore experimentally the weighted contribution of the coherent and random motions, both time-averaged and phased averaged (36 equally spaced phase locked averages) were collected. Then, a triple decomposition technique was used. For simplicity, the equations shown below are given for the streamwise, U_x, velocity component only; however, the same operations were performed on the normal, U_y, velocity component. The time averaged velocity field can be divided into two components as:

(5) $$U_{TA} = \overline{U} + u'$$

Here, U_{TA} is the acquired (using random sampling) velocity, $\overline{U}$ is the mean velocity and u' is the fluctuating component, which consists of the random turbulent fluctuations, u_t, and the coherent fluctuations due to the actuation, $\langle u \rangle$, as follows:

(6) $u' = u_t + \langle u \rangle$

The phase-locked data were obtained by measuring the velocity at 36 phases along the actuation cycle and averaging over all the phases such that the velocity can be expressed as:

(7) $U_{PA} = \overline{U} + \langle u \rangle$

where, U_{PA} is the acquired (using phase-averaging) velocity, $\overline{U}$ is the mean velocity (should be the same as in equation 5, if enough phases are collected), and ,$\langle u \rangle$ is the coherent fluctuations, which can be extracted from equation 7. Note that it was verified that 36 phases were enough for the mean velocities obtained from the time-average and phase-average to be (practically) the same (not shown here). Once $\langle u \rangle$ was found, the random fluctuations could be calculated from Eqs. (5) and (6).

From the triple decomposition, the normal and shear stresses are presented in Figure 3.15, where the total stresses, u'^2, v'^2 and $u'v'$ are shown in figures 3.15a, 3.15d and 3.15g, respectively, the coherent stresses are shown in Figures 3.15b, e and h, and the random fluctuations are given in Figures 3.15c, f and i, respectively. As can be seen, the total stresses concentrate in the area close to the surface and are the highest just downstream of the synthetic jet. The coherent stresses (Figures 3.15b and e) exhibit large concentrations near the jet orifice, suggesting that there the fluctuations are dominated by coherent motions, whereas, farther downstream the strength of the coherent fluctuations diminishes as the coherent fluctuations lose their coherence. The area of higher coherence corresponds directly to the initial emergence of the structures at the orifice and the path of the vortex train seen in figure 3.12. In figures 3.15c and 3.15f, the component random fluctuations are displayed, and the downstream persistence and growth of the randomness can be seen. The contour plot of the total shear stress (figure

3.15g) exhibits concentrated shear near the orifice, which diminishes farther downstream. As can been seen from figures 3.15h and i, the coherent shear stress accounts for most of the total shear, with very little random shear.

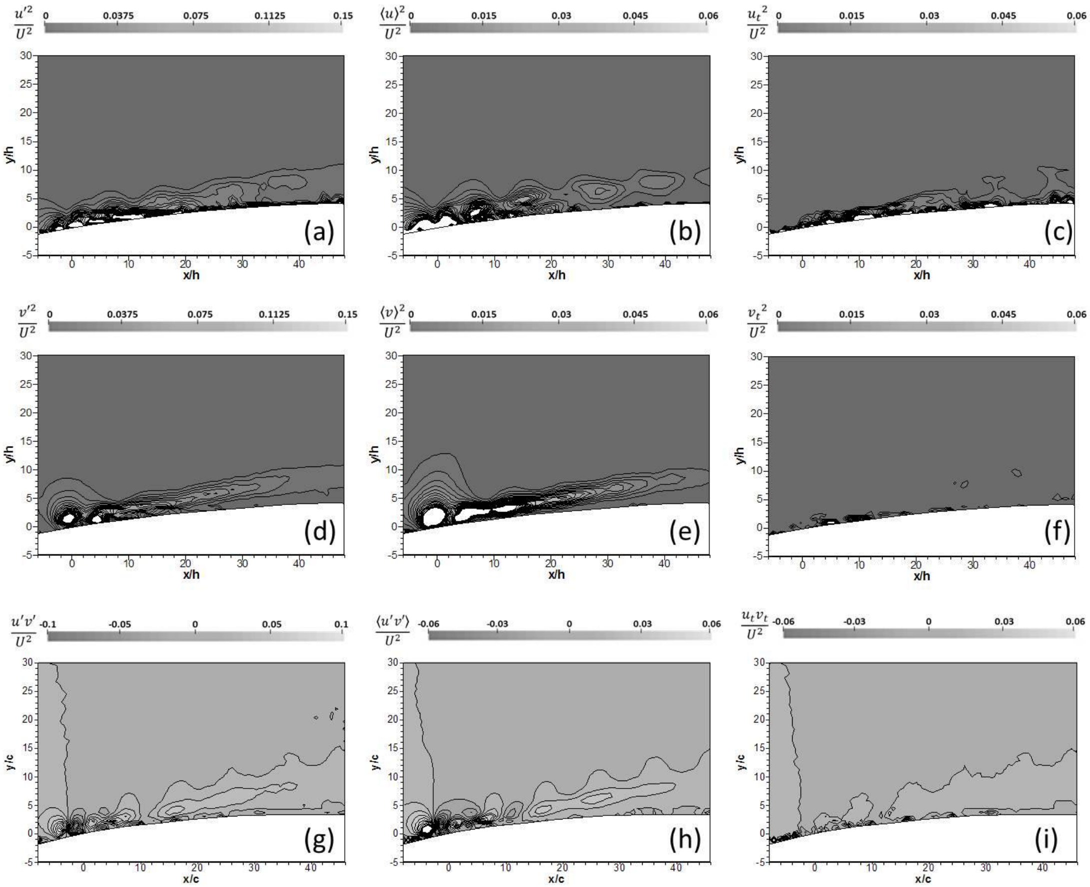

3.15: Black and white contour plots of the dimensionless normal stresses of the streamwise component (a-c), the normal component (d-f) and the shear stresses (g-i); total stresses (a, d, g), coherent stresses (b, e, h) and random stresses (c, f, i) at C_b = 1.2 and Re_c = 100,000.

The total normal stresses (found using equation 6) were then used to compute the turbulent kinetic energy, as follows:

(8) $$k = \frac{1}{2}\left(\overline{u'^2} + \overline{v'^2}\right)$$

where k is the turbulent kinetic energy (TKE), and u'^2 and v'^2 are the total normal stresses. In addition, the coherent and random TKEs were computed using the triple decomposition method, similar to the method used for the normal and shear stresses.

The turbulent kinetic energy is shown in figure 3.16, with the total, coherent, and random contributions depicted in figures 3.16a, 3.16b and 3.16c, respectively. As expected, the highest TKE is near the orifice. Furthermore, the cross-stream extent of the TKE is large near the orifice, whereas slightly downstream it decreases before increasing back to a similar extent as near the jet orifice. Furthermore, the majority of the turbulent kinetic energy is contained in the coherent motions, with only the area very near the airfoil surface containing the random TKE.

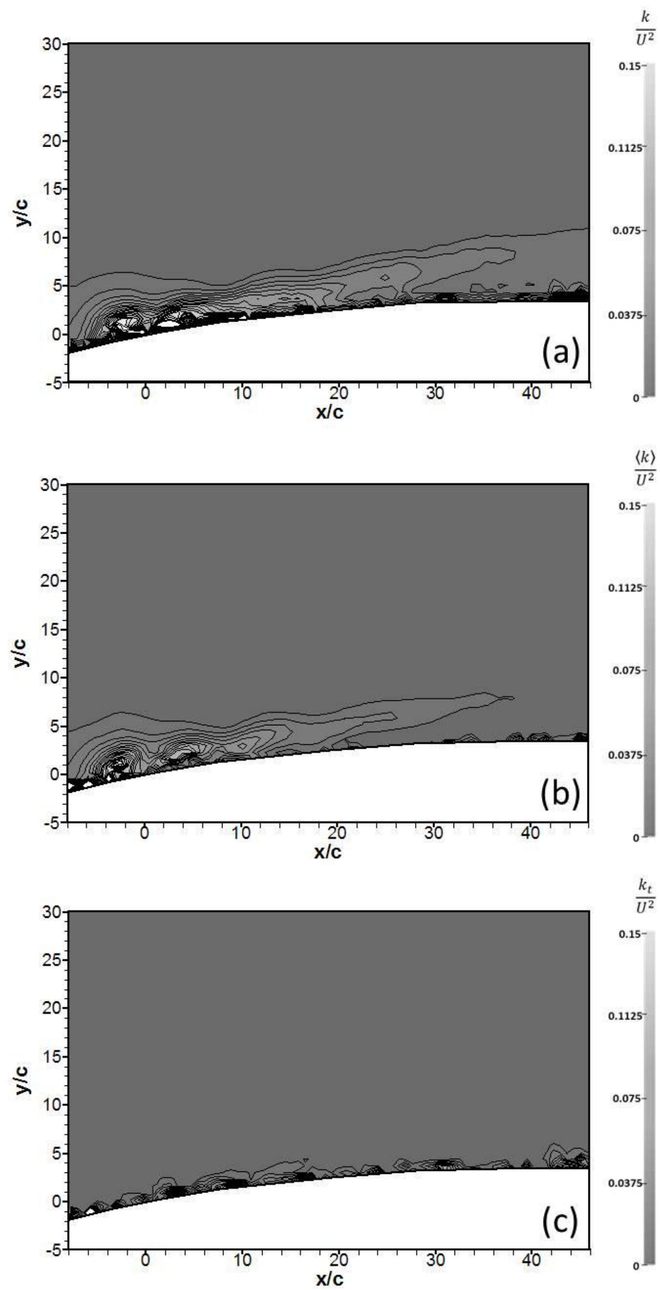

3.16: Black and while contour plots of the normalized total (a), coherent (b), and random turbulent kinetic energy (c) at C_b = 1.2 and Re_c = 100,000.

4. Discussion and Conclusions

This work involved an experimental investigation to study the interaction of a finite-span synthetic jet with a cross-flow over a finite wing (having a cross section of NACA4421) at chord-based Reynolds numbers between 50,000 and 400,000 and a range of angles of attack from 0^0 to 20^0. It was found that at $\alpha = 10^o$, as the Reynolds number increased, the separation location moved toward the trailing edge, with complete reattachment seen at Re = 250,000. When the flow control was applied, for the lower Reynolds number cases, the flow was reattached; however, for the high Reynolds number cases, the effect of the control was to modify the streamlines near surface. For the higher angle of attack cases ($\alpha = 18^o$), the baseline flow was fully separated near the quarter chord for all Reynolds numbers, where the activation of the synthetic jets yielded flow reattachment. Note that the flow was fully reattached at the higher Reynolds numbers whereas only partial separation was achieved at low Reynolds numbers.

Following the parametric study, it was decided to focus on the interaction of the finite-span synthetic jet with the cross-flow at a chord-based Reynolds number of 100,000, and an angle of attack of 0^0, where a range six blowing ratios ($C_b = 0.2$ to $C_b = 1.2$, with an increment of 0.2) was considered.

Three dimensional interactions between the finite-span synthetic jet and cross-flow were analyzed based on time-averaged, phase-averaged and instantaneous flow fields. Experiments provided results for six different blowing ratios. Emphasis was placed on flow structures along with their interactions and evolution in the vicinity of the synthetic jet. It was found that in the low momentum coefficient cases, 2-D spanwise rollers formed near the slit in each jet cycle; however, due to the finite-span of the slit streamwise vortices developed at the edge of the slit. Furthermore, the cross-flow accelerates around the edge of the slit and develops spanwise velocity components. Due to which the 2-D spanwise rollers are perturbed leading to formation of small and organized secondary flow structures farther downstream in the form of multiple distinct streak-like flow structures in the mean flow. On the other hand, in the high blowing ratio cases turbulent vortical structures were dominant that lead to larger spanwise structures, or lobe-like pattern, in the mean flow, where three-dimensionalities were formed immediately downstream of the jet slit. In all cases the spanwise extent of the coherent structures reduced with downstream distance; the decrease was more for cases with higher blowing ratio. Similar flow patterns were observed in earlier studies on finite-span synthetic jets without a cross-flow, e.g., Amitay & Cannelle (2006).

Spatial and temporal evolution of flow structures were also studied with the help of cross-stream planes at different locations, and phase-averaged flow fields at six different phases. It was found that in low-range cases (with C_b = 0.2 and C_b = 0.4) well-organized structures existed in the form of multiple distinct streamwise-oriented secondary vortical structures. In the mid-blowing ratio range, combined features of the low-range (near the slit) and high-range (in downstream locations) were found and the pair of counter-rotating vortices issued in the same jet cycle collided with each other. In the high-bowling ratio range, a train of counter-rotating coherent vortices existed that lifted-off the surface as they advected downstream.

The random and coherent fluctuations in the flow field were explored through the collection of 36 phase locked averages and an ensemble average, and then performing a triple decomposition on these data. It was shown that near the jet the flow consists of predominately coherent fluctuations, where the vortical structures produced by the synthetic jet are the strongest, and the random motions gradually overtake away from the orifice in the streamwise direction. In the vertical direction, there is an abrupt drop off in the coherent motions as the maximum height of structures produced is reached.

5. Future Work

The current work has focused on an unswept wing and only in the vicinity of a single actuator. The piezo disks that were used in this research are also problematic, with a high failure rate and very low tolerances. Therefore, the future work should be to first redesign the actuators to use more robust disks. It is also propose to explore the effect of a sweep to allow further exploration of not only jet/freestream interactions, but also the effect of the spanwise component of velocity on the interaction. This would mean a much larger volume reconstruction, including multiple actuators, and consequently a much better understanding of the jet/flow interaction, which will lead to a better actuation design and thus larger effect of the flow and the global aerodynamic properties.

6. References

Abbott, I.H. & von Doenhoff, A.E. (1959). *Theory of Wing Sections: Including a Summary of Airfoil Data*. New York, NY: Dover Publications Inc.

Amitay, M. & Cannelle, F. (2006). Evolution of Finite Span Synthetic Jets. *Physics of Fluids, 18,* 054101.

Amitay, M. & Glezer, A. (2002a). Role of Actuation Frequency in Controlled Flow Reattachment over a Stalled Airfoil. *AIAA Journal*, *40,* 209-216.

Amitay, M. & Glezer, A. (2002b). Controlled Transients of Flow Reattachment over Stalled Airfoils. *International Journal of Heat and Fluid Flow, 23,* 690-699.

Amitay, M. & Glezer, A. (2006). Flow Transients Induced on a 2-D Airfoil by Pulse-Modulated Actuation. *Experiments in Fluids, 40,* 329–331.

Amitay, M., Honohan, A., Trautman, M. & Glezer, A. (1997). Modification of the Aerodynamic Characteristics of Bluff Bodies Using Fluidic Actuators. *AIAA Paper 97-2004*.

Amitay, M., Horvath, M., Michaux, M. & Glezer, A. (2001a). Virtual Aerodynamic Shape Modification at Low Angles of Attack using Synthetic Jet Actuators. *AIAA Paper 2001-2975*.

Amitay, M., Kibens, V., Parekh, D.E. & Glezer, A. (1999). Flow Reattachment Dynamics over a Thick Airfoil Controlled by Synthetic Jet Actuators. *AIAA Paper 99-1001*.

Amitay, M., Pitt, D. & Glezer, A. (2002c). Separation Control in Duct Flows. *Journal of Aircraft*, *39,* 616-620.

Amitay, M., Smith, D.R., Kibens, V., Parekh, D.E. & Glezer, A. (2001b). Modification of the Aerodynamics Characteristics of an Unconventional Airfoil Using Synthetic Jet Actuators. *AIAA Journal, 39,* 361-370.

Cannelle, F. and Amitay, M. (2007). Transitory Behavior of a Finite Span Synthetic Jet. *Physics of Fluids*, *19,* 094108.

Cater, J.E. and Soria, J. (2002). The Evolution of Round Zero-Net-Mass-Flux Jets. *Journal of Fluid Mechanics, 472,*167-200.

Chatlynne, E., Rumigny, N., Amitay, M. & Glezer, A. (2001). Virtual Aero-Shaping of a Clark-Y Airfoil using Synthetic Jet Actuators. *AIAA Paper 2001-0732*.

Chen, F.-J., Yao, C., Beeler, G.B., Bryant, R.G. & Fox, R.L. (2000). Development of Synthetic Jet Actuators for Active Flow Control at NASA Langley. *AIAA Paper 2000-2405*.

Ciuryla, M., Liu, Y., Farnsworth, J., Kwan, C. & Amitay, M. (2007). Flight Control Using Synthetic Jets on a Cessna 182 Model. *Journal of Aircraft*, *44,* 642-653.

Crook, A., Sadri, A.M. & Wood, N.J. (1999). The Development and Implementation of Synthetic Jets for the Control of Separated Flow. *AIAA Paper 99-3176*.

Crook, A. & Wood, N.J. (2001). Measurements and Visualizations of Synthetic Jets. *AIAA Paper 2001-0145*.

Cui, J. & Agarwal, R.K. (2005). 3-D CFD Validation of an Axisymmetric Jet in Cross-Flow (NASA Langley Workshop Validation: Case 2). *AIAA Paper 2005-1112*.

Cui, J. & Agarwal, R.K. (2006). Three-dimensional Computation of a Synthetic Jet in Quiescent Air. *AIAA Journal, 44,* 2857-2865.

Dandois, J., Garnier, E. & Sagaut, P. (2006). Unsteady Simulation of a Synthetic Jet in a Crossflow. *AIAA Journal, 44,* 225-238.

Farnsworth, J.A.N., Vaccaro, J.C. & Amitay, M. (2008). Active Flow Control at Low Angles of Attack: Stingray Unmanned Aerial Vehicle. *AIAA Journal, 46,* 2530-2544.

Gallas, Q., Holman, R., Nishida, T., Carroll, B., Sheplak, M. & Cattafesta, L. (2003). Lumped Element Modeling of Piezoelectric-Driven Synthetic Jet Actuators. *AIAA Journal, 41*, 240-247.

Gilarranz, J.L., Traub, L.W. & Rediniotis, O.K. (2005). A New Class of Synthetic Jet Actuators - Part II: Application to Flow Separation Control. *ASME Journal of Fluids Engineering, 127,* 377-387.

Glezer, A. & Amitay, M. (2002). Synthetic Jets. *Annual Review of Fluid Mechanics, 34,* 503-529.

Glezer, A., Amitay, M. & Honohan, A. (2005). Aspects of Low- and High-Frequency Actuation for Aerodynamic Flow Control. *AIAA Journal, 43,* 1501-1511.

Gordon, M. & Soria, J. (2002). PIV Measurements of a Zero-Net-Mass-Flux Jet in Cross Flow. *Experiments in Fluids, 33,* 863-872.

Greenblatt, D. & Washburn, A. (2008). Influence of Finite Span and Sweep on Active Flow Control Efficacy. *AIAA Journal, 46,* 1675-1694.

He., Y., Cary, A.W. & Peters, D.A. (2001). Parametric and Dynamic Modeling for Synthetic Jet Control of a Post-Stall Airfoil. *AIAA Paper 2001-0733*.

Ho., C.-M. & Huerre, P. (1984). Perturbed Free Shear Layers. *Annual Review of Fluid Mechanics, 16,* 365-422.

Iai, T., Motosuke M. & Honami, S. (2009). Vortex Behavior of Vertical and Inclined Synthetic Jet in Cross Flow at Low Reynolds Number. *AIAA Paper 2009-4178*.

Jabbal, M. & Zhong, S. (2008). The Near Wall Effect of Synthetic Jets in a Boundary Layer. *International Journal of Heat and Fluid Flow, 29,* 119-130.

Kotapati, R.B., Mittal, R. & Cattafesta III, L.N. (2007). Numerical Study of a Transitional Synthetic Jet in Quiescent External Flow. *Journal of Fluid Mechanics, 581*, 287-321.

Kral, L.D., Donovan, J.F., Cain, A.B. & Cary, A.W. (1997). Numerical Simulation of Synthetic Jet Actuators. *AIAA Paper 97-1824*.

Lee, C.Y. & Goldstein, D.B. (2002). Two-dimensional Synthetic Jet Simulation. *AIAA Journal, 40,* 510-516.

Maldonado, V., Farnsworth, J., Gressick, W. & Amitay, M. (2009). Active Control of Flow Separation and Structural Vibrations of Wind Turbine Blades. *Wind Energy, 13,* 221-237.

Mallinson, S.G., Hong, G. & Reizes, J.A. (1999). Some Characterstics of Synthetic Jets. *AIAA Paper 99-3651*.

Mallinson, S.G., Reizes, J.A., Hong, G. & Westbury, P.S. (2004). Analysis of Hot-wire Anemometry Data Obtained in a Synthetic Jet Flow. *Experimental Thermal and Fluid Science*, *28,* 265-272.

Milanovic, I.M. & Zaman, K.B.M.Q. (2003). Synthetic Jets in Cross-Flow. Part II: Jets from Orifices of Different Geometry. *AIAA Paper 2003-3715*.

Milanovic, I.M., Zaman, K.B.M.Q. & Rumsey, C.L. (2005). An Isolated Circular Synthetic Jet in Cross-Flow at Low Momentum-Flux Ratio. *AIAA Paper 2005-1110*.

Mittal, R. & Rampunggoon, P. (2002). On the Virtual Aeroshaping Effect of Synthetic Jets. *Physics of Fluids, 14,* 1533.

Mittal, R., Rampunggoon, P. & Udaykumar, H.S. (2001). Interaction of a Synthetic Jet with a Flat Plate Boundary Layer. *AIAA Paper 2001-2773*.

Oster, D. & Wygnanski, I. (1982). The Forced Mixing Layer between Parallel Streams. *Journal of Fluid Mechanics, 123,* 91-130.

Parekh, D.E., Williams, S.P., Amitay, M., Glezer, A., Washburn, A.E., Gregory, I.M. & Scott, R.C. (2004). Active Flow Control on the Stingray UAV: Aerodynamic Forces and Moments. *AIAA Paper 2003-4002*.

Pope, S.B. (2000). *Turbulent Flows*. Cambridge, England: Cambridge University Press.

Prasad, A.K. & Jensen, K. (1995). Scheimpflug stereocamera for particle image velocimetry in liquid flows. *Applied Optics, 34,* 7092-7099.

Rizzetta, D.P., Stanek, M.J. & Visbal, M.R. (1999). Numerical Simulation of Synthetic-Jet Flowfields. *AIAA Journal, 37,* 919-927.

Roberts, F.A. (1985). *Effects of Periodic Disturbances on Structure of Mixing in Turbulent Shear Layers and Wakes*. PhD Thesis: California Institute of Technology.

Sahni, O., Wood, J., Jansen, K.E. & Amitay, M. (2011). Three Dimensional Interactions between a Finite-Span Synthetic Jet and a Cross-Flow. *Journal of Fluid Mechanics, 671,* 254-287.

Sauerwein, S.C. & Vakili, A.D. (1999). An Experimental Study of Zero-Mass Jets in Crossflow. *AIAA Paper 99-0668*.

Schaeffler, N.W. & Jenkin, L.N. (2006). Isolated Synthetic Jet in Crossflow: Experimental Protocols for a Validation Dataset. *AIAA Journal, 44,* 2846-2856.

Seifert, A., Bachar, T., Koss, D., Shepshelovich, M. & Wygnanski, I. (1993). Oscillatory Blowing: A Tool to Delay Boundary-Layer Separation. *AIAA Journal, 31,* 2052-2060.

Smith, B.L. & Glezer, A. (1998). The Formation and Evolution of Synthetic Jets. *Physics of Fluids, 10,* 2281-2297.

Smith, B.L. & Glezer, A. (2002). Jet Vectoring using Synthetic Jets. *Journal of Fluid Mechanics, 458,* 1-34.

Smith, D.R. (2002). Interaction of a Synthetic Jet with a Crossflow Boundary Layer. *AIAA Journal, 40,* 2277-2288.

Timor, I., Ben-Hamou, E., Guy, Y. & Seifert, A. (2007). Maneuvering Aspects and 3D Effects of Active Airfoil Flow Control. *Flow, Turbulence and Combustion, 78,* 429-443.

Timoshenko, S. & Woinowsky-Krieger, S. (1959). *Theory of Plates and Shells*. New York, NY: McGraw-Hill.

Westerweel, J. (2000). Theoretical analysis of the measurement precision in particle image velocimetry. *Experiments in Fluids, 29,* 3-12

Wu, D.K.L. & Leschziner, M.A. (2009). Large-Eddy Simulations of Circular Synthetic Jets in Quiescent Surroundings and in Turbulent Cross-Flow. *International Journal of Heat and Fluid Flow, 30,* 421-434.

Wygnanski, I. (2000). Some New Observations Affecting the Control of Separation by Periodic Excitation. *AIAA Paper 2000-2314*.

You, D. & Moin, P. (2008). Active Control of Flow Separation over an Airfoil using Synthetic Jets. *Journal of Fluids and Structures, 24,* 1349-1357.

Zaman, K.B.M.Q. & Milanovic, I.M. (2003). Synthetic Jets in Cross-Flow. Part 1: Round Jet. *AIAA Paper 2003-3714.*

Zhou, J. & Zhong, S. (2009). Numerical Simulation of the Interaction of a Circular Synthetic Jet with a Boundary Layer. *Computers and Fluids, 38,* 393-405.